Observation-Based Source Terms in the Third-Generation Wave Model WAVEWATCH III: Updates and Verification

QINGXIANG LIU,[a] W. ERICK ROGERS,[b] ALEXANDER V. BABANIN,[a] IAN R. YOUNG,[a] LEONEL ROMERO,[c] STEFAN ZIEGER,[d] FANGLI QIAO,[e] AND CHANGLONG GUAN[f]

[a] *Department of Infrastructure Engineering, University of Melbourne, Melbourne, Victoria, Australia*
[b] *Naval Research Laboratory, Stennis Space Center, Mississippi*
[c] *Earth Research Institute, University of California, Santa Barbara, Santa Barbara, California*
[d] *Bureau of Meteorology, Melbourne, Victoria, Australia*
[e] *First Institute of Oceanography, Ministry of Natural Resources, Qingdao, China*
[f] *Physical Oceanography Laboratory, Ocean University of China, and Pilot National Laboratory for Marine Science and Technology, Qingdao, China*

(Manuscript received 27 June 2018, in final form 28 November 2018)

ABSTRACT

The observation-based source terms available in the third-generation wave model WAVEWATCH III (i.e., the ST6 package for parameterizations of wind input, wave breaking, and swell dissipation terms) are recalibrated and verified against a series of academic and realistic simulations, including the fetch/duration-limited test, a Lake Michigan hindcast, and a 1-yr global hindcast. The updated ST6 not only performs well in predicting commonly used bulk wave parameters (e.g., significant wave height and wave period) but also yields a clearly improved estimation of high-frequency energy level (in terms of saturation spectrum and mean square slope). In the duration-limited test, we investigate the modeled wave spectrum in a detailed way by introducing spectral metrics for the tail and the peak of the omnidirectional wave spectrum and for the directionality of the two-dimensional frequency–direction spectrum. The omnidirectional frequency spectrum $E(f)$ from the recalibrated ST6 shows a clear transition behavior from a power law of approximately f^{-4} to a power law of about f^{-5}, comparable to previous field studies. Different solvers for nonlinear wave interactions are applied with ST6, including the Discrete Interaction Approximation (DIA), the more expensive Generalized Multiple DIA (GMD), and the very expensive exact solutions [using the Webb–Resio–Tracy method (WRT)]. The GMD-simulated $E(f)$ is in excellent agreement with that from WRT. Nonetheless, we find the peak of $E(f)$ modeled by the GMD and WRT appears too narrow. It is also shown that in the 1-yr global hindcast, the DIA-based model overestimates the low-frequency wave energy (wave period $T > 16$ s) by 90%. Such model errors are reduced significantly by the GMD to ~20%.

1. Introduction

In deep water, the evolution of wind-generated ocean waves can be described by the radiative transfer equation (e.g., Komen et al. 1994; Young 1999):

$$\frac{dN}{dt} = \frac{S_{\text{in}}(+S_{\text{swl}}) + S_{\text{ds}} + S_{\text{nl}} + \cdots}{\sigma}, \tag{1}$$

where $N(k, \theta; \mathbf{x}, t) = F(k, \theta; \mathbf{x}, t)/\sigma$ is the wave action density spectrum, $F(k, \theta; \mathbf{x}, t)$ is the two-dimensional wavenumber spectrum, σ is the intrinsic (radian) frequency, k is the wavenumber, and θ is the propagation direction of wave energy. For deep water the dispersion relation is

$$\sigma^2 = gk, \tag{2}$$

and g is gravitational acceleration. The RHS of (1) represents different physical sources and fluxes of wave energy, including the wind input term S_{in}, wave breaking term S_{ds}, nonlinear wave–wave interaction S_{nl}, and swell decay S_{swl}, among others (Cavaleri et al. 2007; Holthuijsen 2007; Cavaleri et al. 2018).

Supplemental information related to this paper is available at the Journals Online website: https://doi.org/10.1175/JPO-D-18-0137.s1.

Corresponding author: Qingxiang Liu, qingxiang.liu@unimelb.edu.au

DOI: 10.1175/JPO-D-18-0137.1

The 3-yr field experiment carried out in Lake George, New South Wales, Australia, in 1997–2000 (Young et al. 2005; Donelan et al. 2005) revealed various novel features of wave dynamics. For the wind input S_{in}, the main novel features (Donelan et al. 2006) are the following: 1) S_{in} is a nonlinear function of the wave spectrum because the growth rate γ depends on wave steepness and hence on the spectrum itself; 2) the growth rate γ slows down in extreme conditions because of the flow separation (in relative terms; the growth still increases as the wind increases, but not as fast as one would expect by extrapolating the measurement in moderate wind-forcing conditions); and 3) wind input doubles over a breaking wave and hence can increase if the breaking rates are substantial (Babanin et al. 2007). For the whitecapping dissipation term S_{ds}, the novel features are as follows: 1) the threshold for inherent wave breaking demonstrates its existence in terms of (significant) wave steepness (Banner et al. 2000; Babanin et al. 2001), and Babanin and Young (2005) established dimensionless value for such threshold across the entire spectrum; 2) the two-phase behavior of S_{ds} is noteworthy: at any frequency the breaking can happen due to inherent reasons, but above the spectral peak the breaking is also enhanced due to the influence of longer waves on shorter ones (Babanin and Young 2005; Young and Babanin 2006); 3) the direct dependence of S_{ds} on the wind speed when U_{10} (the wind speed at 10 m above the sea surface) exceeds 14–15 m s^{-1} (Manasseh et al. 2006); and 4) the directional distribution of S_{ds} is bimodal rather than isotropic (Young and Babanin 2006).

These Lake George observations resulted in a new set of source functions for wind input S_{in} (Donelan et al. 2006; Babanin et al. 2007) and whitecapping dissipation S_{ds} (Babanin and Young 2005; Young and Babanin 2006), which were tested in academic models (Tsagareli et al. 2010; Babanin et al. 2010) and subsequently implemented in Simulating Waves Nearshore (SWAN; Booij et al. 1999) and WAVEWATCH III (WW3; Tolman 1991) by Rogers et al. (2012, hereafter RBW12) and Zieger et al. (2015, hereafter ZBRY15), respectively. Practical modeling also required introduction of further observation-based physics such as swell dissipation S_{swl} (Babanin 2006, 2011; Young et al. 2013) and negative wind input (ZBRY15; Aijaz et al. 2016; Liu et al. 2017). Once the waves stop breaking, the dissipation continues, but due to a different reason: turbulence production by wave orbital motion (i.e., the so-called swell decay S_{swl}) (Babanin 2006; Babanin and Haus 2009; Young et al. 2013). Note that other mechanisms responsible for S_{swl} based on the interaction of ocean waves and upper ocean turbulence or air turbulence are also available in the literature (e.g., Teixeira and Belcher 2002; Ardhuin and Jenkins 2006; Ardhuin et al. 2009). This complete set of new physics ready for practical forecast and hindcast received the name of ST6[1] in 2014 and 2016 public releases of WW3 (WAVEWATCH III Development Group 2016, hereafter T16). Besides, ST6 is now formally part of the SWAN model as well (SWAN Team 2018, version 41.20A). Further academic developments related to ST6 included a new nonlinear interaction term based on the general kinetic equation (Gramstad and Babanin 2016), modules for wave–current interactions (Rapizo et al. 2017), infragravity waves (Nose et al. 2017), and wave–ice interactions (to be released in the 2019 version of WW3).

Since its implementation in SWAN and WW3, this unique source term package, ST6, of $S_{in} + S_{ds} + S_{swl}$ has been proven skillful for different spatial scales and under different weather conditions (e.g., ZBRY15; Aijaz et al. 2016; van Vledder et al. 2016; Liu et al. 2017). ZBRY15 (their Fig. 5) and Stopa et al. (2016, hereafter SABZ16, their Fig. 7), however, also suggested that ST6 was inclined to overestimate the energy level of the high-frequency tail of the spectrum, indicating an inaccurate balance of different source terms in this specific frequency range.

As will be shown in this paper, this shortcoming can be solved by increasing the wind input S_{in} slightly and then recalibrating tunable parameters of S_{ds} [i.e., a_1 and a_2 in (9) and (10)]. From a practical point of view, a relatively stronger input allows a higher dissipation, which in turn pulls the overestimated spectral tail down to the correct energy level. Through detailed analyses of academic and realistic simulations performed with WW3 (version 5.16[2]; T16), we demonstrate that the recalibrated ST6 package not only performs well in predicting commonly used bulk wave parameters (e.g., significant wave height H_s and wave periods; appendix A), but also yields a clearly improved estimation of the high-frequency energy level [or specifically, the saturation spectrum $B(f)$ in (21) and mean square slope $\langle s^2 \rangle$; appendix A]. Besides, the updated ST6 is also able to produce a realistic transition behavior from $E(f) \propto f^{-4}$ to $E(f) \propto f^{-5}$, where $E(f)$ is the omnidirectional frequency spectrum.[3]

The Discrete Interaction Approximation of S_{nl} (DIA; Hasselmann et al. 1985) is the crucial component permitting routine application of third-generation wave

[1] The third novel feature of S_{in} and the fourth feature of S_{ds} are not implemented in ST6 yet.

[2] With minor modification of ST6 codes.

[3] $\propto$: approximately proportional to.

models (e.g., Hasselmann et al. 1988; Tolman 1991). It however also has some well-known shortcomings as an approximation (see an extended discussion about this issue in section 2b). To investigate the errors in spectral wave models attributable to the DIA, we first specifically optimize another more accurate nonlinear solver, that is, the Generalized Multiple DIA (GMD; Tolman 2013) for ST6, and then conduct a thorough comparison of model simulations with these two different nonlinear solvers. The most prominent advantage of the GMD-based model over the DIA-based model, as later illustrated in this paper, is that the former shows a much higher accuracy in simulating the energy of long-period waves ($T > 16$ s). The computational expense of the GMD approach used here, however, is about 5 times larger than that of the DIA.

This paper is organized as follows. Section 2 provides a brief overview of ST6 source functions ($S_{\text{in}} + S_{\text{ds}} + S_{\text{swl}}$) and the four-wave resonant interactions S_{nl}. Section 3 describes the updates of ST6 over its predecessor, particularly focusing on the retuning procedure. Section 4 presents a detailed analysis of modeled wave spectra from duration-limited simulations, followed by a thorough validation of model performance with a 1-yr global hindcast in section 5. Conclusions in section 6 finalize this paper.

2. Parameterizations

a. ST6 source term package

A brief overview of the ST6 source terms is given here for completeness. The reader is referred to RBW12 and ZBRY15 and references therein for more details.

1) WIND INPUT S_{in}

The wind input parameterization S_{in}, formulated by Donelan et al. (2006), is given as follows:

$$S_{\text{in}}(k,\theta) = \frac{\rho_a}{\rho_w}\sigma(k)\gamma(k,\theta)F(k,\theta), \tag{3}$$

$$G(k,\theta) = \mu_1 - \mu_2\left\{1 + \tanh\left[\mu_3\sqrt{B_n(k)}\,W^2(k,\theta) - \mu_4\right]\right\}, \text{ and} \tag{4}$$

$$\gamma(k,\theta) = \alpha_{\text{in}}G(k,\theta)\sqrt{B_n(k)}W^2(k,\theta), \tag{5}$$

where ρ_a and ρ_w are air and water densities, $W(k,\theta) = U_s\cos(\theta-\theta_u)/c(k) - 1$ is the wind forcing parameter, U_s is the scaling wind speed, $c(k) = \sigma/k$ is the phase velocity, and $B_n(k) = B(k)A(k)$ is a spectral measure of wave steepness—the saturation spectrum $B(k) = k^3F(k)$ (Phillips 1984) normalized by the spreading function A [$\mathscr{O}(1)$; Babanin and Soloviev 1998b]. Also, $G(k,\theta)$ represents the degree of flow separation (whether the full separation occurs or not) and α_{in} is the wind growth parameter:

$$\alpha_{\text{in}} = \begin{cases} 1, & \text{for } W(k,\theta) \geq 0 \\ -a_0, & \text{for } W(k,\theta) < 0 \end{cases}. \tag{6}$$

Here a_0 is a tuning parameter controlling the strength of negative wind input (ZBRY15; Liu et al. 2017, and references therein). The specific values of the four parameters μ_i, $i = 1, \ldots, 4$ in (4) vary with the scaling wind speed U_s adopted in $W(k,\theta)$. For $U_s = U_{10}$, Donelan et al. (2006) suggested

$$\mu_1 = 2.8, \quad \mu_2 = 1.0, \quad \mu_3 = 10, \quad \text{and} \quad \mu_4 = 11.$$

The wave model community, however, prefers u_* scaling in order to assure a consistent fetch law across different wind speeds (Komen et al. 1994, p. 253), where u_* is the friction velocity. Therefore, RBW12 advocated using an approximation

$$U_s = U_{10} \simeq \Upsilon u_*, \quad \text{and} \quad \Upsilon = 28 \tag{7}$$

by following Komen et al. (1984).

2) WAVE BREAKING S_{ds}

The wave breaking parameterization S_{ds} of the ST6 package incorporates two different mechanisms: 1) the inherent wave breaking $T_1(k,\theta)$ occurring at each frequency once the steepness of that wave component exceeds a threshold value (Banner et al. 2000; Babanin et al. 2001) and 2) the induced breaking of relatively short waves $T_2(k,\theta)$ due to the modulation of longer waves (Donelan 2001; Young and Babanin 2006). The source term reads (RBW12; ZBRY15)

$$S_{\text{ds}}(k,\theta) = T_1(k,\theta) + T_2(k,\theta), \tag{8}$$

$$T_1(k,\theta) = -a_1 f\left[\frac{\Delta(k)}{F_T(k)}\right]^{p_1}F(k,\theta), \quad \text{and} \tag{9}$$

$$T_2(k,\theta) = -a_2\int_{f_{\text{min}}}^{f}\left[\frac{\Delta(k)}{F_T(k)}\right]^{p_2}dfF(k,\theta), \tag{10}$$

where a_1, a_2, p_1, and p_2 are tunable parameters, f_{min} is the lowest discrete frequency defined in the spectral grid, $F_T(k) = B_T/k^3$ is the spectral threshold, $B_T = 0.035^2$ is the dimensionless saturation-threshold value, and $\Delta(k) = F(k) - F_T(k)$ is the exceedance level (Babanin et al. 2010). RBW12 found that highly nonlinear T_1 and T_2 are required to balance the strong wind

input [(3)] beyond the spectral peak. This was achieved by setting $p_1 = p_2 = 4$.

3) SWELL DISSIPATION S_{swl}

The swell dissipation term S_{swl} of ST6 characterizes the loss of wave energy as a result of the turbulence production by nonbreaking surface waves (Babanin 2006; Babanin and Haus 2009). According to Babanin (2011) and Young et al. (2013), ZBRY15 implemented S_{swl} as

$$S_{swl}(k,\theta) = -\frac{2}{3} b_1 \sigma(k) \sqrt{B_n(k)} F(k,\theta), \tag{11}$$

where the dimensionless proportionality coefficient b_1 is hypothesized to be steepness-dependent in the following way:

$$b_1 = \frac{B_1 H_s k_p}{2}. \tag{12}$$

Here k_p is the peak wavenumber and B_1 is a tunable scaling coefficient. Note that S_{swl} is applied to both wind sea and swell. But in the context of wind sea, it does not contribute significantly to the source term balance (e.g., ZBRY15).

b. Nonlinear wave–wave interactions S_{nl}

Hasselmann (1962) pointed out that four wave components satisfying the resonance condition

$$\begin{cases} \mathbf{k}_1 + \mathbf{k}_2 = \mathbf{k}_3 + \mathbf{k}_4 \\ \sigma_1 + \sigma_2 = \sigma_3 + \sigma_4 \end{cases}, \tag{13}$$

could exchange energy and momentum, where $\mathbf{k}$ is the wavenumber vector. The set of these four waves is also known as a quadruplet. The nonlinear term $S_{nl}(k, \theta)$ describes the redistribution of wave energy over the spectrum resulted from such resonant wave–wave interactions. The important role of S_{nl} in the evolution of wave spectrum is well founded (e.g., Hasselmann et al. 1973; Young and van Vledder 1993). The computation of its exact solutions, such as by the Webb–Resio–Tracy (WRT) method (Webb 1978; Tracy and Resio 1982; Resio and Perrie 1991; van Vledder 2006), however, is extremely time-consuming, and this prohibits its applicability to large-scale wave hindcasting and forecasting. Hasselmann et al. (1985) proposed the DIA approach to overcome this difficulty by accounting for interaction contributions for a *single* representative quadruplet only, defined by (13) and

$$\begin{cases} \mathbf{k}_1 = \mathbf{k}_2 \\ \sigma_3 = (1+\lambda)\sigma_1, \\ \sigma_4 = (1-\lambda)\sigma_1 \end{cases} \tag{14}$$

where λ is a free shape parameter. The DIA is not only several orders of magnitude more efficient (e.g., Tolman 2013, his Table 4), but also retains the dominant features of the exact solutions (Hasselmann et al. 1985; Young et al. 1987). Accordingly, it has been widely used for decades in third-generation spectral wave models (Hasselmann et al. 1988; Tolman 1991; Booij et al. 1999).

Nonetheless, the shortcomings of DIA have also been extensively discussed. First, the two lobes of S_{nl} beyond the peak frequency f_p—one negative lobe close to f_p and one positive lobe at higher frequencies—computed by the DIA are clearly different from the exact solutions (Hasselmann et al. 1985; Cavaleri et al. 2007). As a result, the DIA may not be able to yield a correct form of the equilibrium range (f^{-4}) of the wind wave spectra (Resio et al. 2016). Second, wave spectra from the DIA are too broad in both frequency and directional space (e.g., Young et al. 1987; Cavaleri et al. 2007; Rogers and van Vledder 2013). Third, the DIA could fail to reproduce the directional bimodality of short waves because of its tendency to misplace the two lobes of S_{nl} beyond f_p (van der Westhuysen et al. 2007; Cavaleri et al. 2007). Finally, it is also noteworthy that under hurricane conditions the DIA may give rise to ~20% errors in the simulated H_s, as shown in Tolman (2013) and Liu et al. (2017). Liu et al. (2017, their Fig. 13) also demonstrated that for cross swell the low-frequency wave energy simulated by DIA is clearly higher than that by WRT.

Tolman (2013) developed a more accurate parameterization of S_{nl} (i.e., the GMD) by expanding the DIA in several ways. The definition of the representative quadruplet [(14)] is extended as follows:

$$\begin{cases} \sigma_2 = \dfrac{1-\mu}{1+\mu}\sigma_1 \\ \sigma_3 = \dfrac{1+\lambda}{1+\mu}\sigma_1 \\ \sigma_4 = \dfrac{1-\lambda}{1+\mu}\sigma_1 \\ \theta_{12} = \arccos\dfrac{\mathbf{k}_1 \cdot \mathbf{k}_2}{k_1 k_2} \end{cases}, \tag{15}$$

where μ is the second shape parameter and θ_{12} is the angle between $\mathbf{k}_1$ and $\mathbf{k}_2$. Clearly, (14) is a simplified form of (15) for $\mu = 0$ and $\theta_{12} = 0°$. Another important feature of the GMD is its capacity of incorporating interaction contributions for multiple representative quadruplets, rather than one quadruplet only by the DIA. For brevity, other advantageous features of the GMD over the DIA are not described here. The reader is referred to Tolman (2010), Tolman (2013), and

Tolman and Grumbine (2013) for further details. These three studies showed that the accuracy of the GMD increases with increasing numbers of free parameters used in (15) [i.e., one-parameter (λ), two-parameter (λ, μ), and three-parameter (λ, μ, θ_{12}) quadruplet layout] and increasing numbers of quadruplets n_q. For the three-parameter (λ, μ, θ_{12}) quadruplet definition, the improvement of GMD accuracy will saturate at $n_q = 5$ or 6. Considering this, we chose the GMD configuration with five quadruplets and a three-parameter quadruplet definition[4] in our following analysis. For convenience, we will also simply refer to this specific GMD configuration as GMD. Figure 1, as an example, clearly illustrates the differences in quadruplet layouts used by the DIA (Fig. 1a) and the GMD (Fig. 1b). Note that only the deep scaling function of the GMD is used in our manuscript, which represents "weak" four-wave nonlinear interactions in deep water and intermediate depths for $kd \geq 0.75$ (d is water depth; Tolman 2013). This is comparable to the applicable range of the DIA and its kd-dependent scaling relation for $kd \geq 0.8$ (e.g., Hasselmann and Hasselmann 1985; Hasselmann et al. 1988). The application of ST6 with other nonlinear solvers such as the simplified Research Institute for Applied Mechanics (RIAM; Komatsu and Masuda 1996; Tamura et al. 2008) and two-scale approximation (TSA; Resio and Perrie 2008; Perrie et al. 2013) is beyond the scope of this paper, and therefore may be pursued in the future.

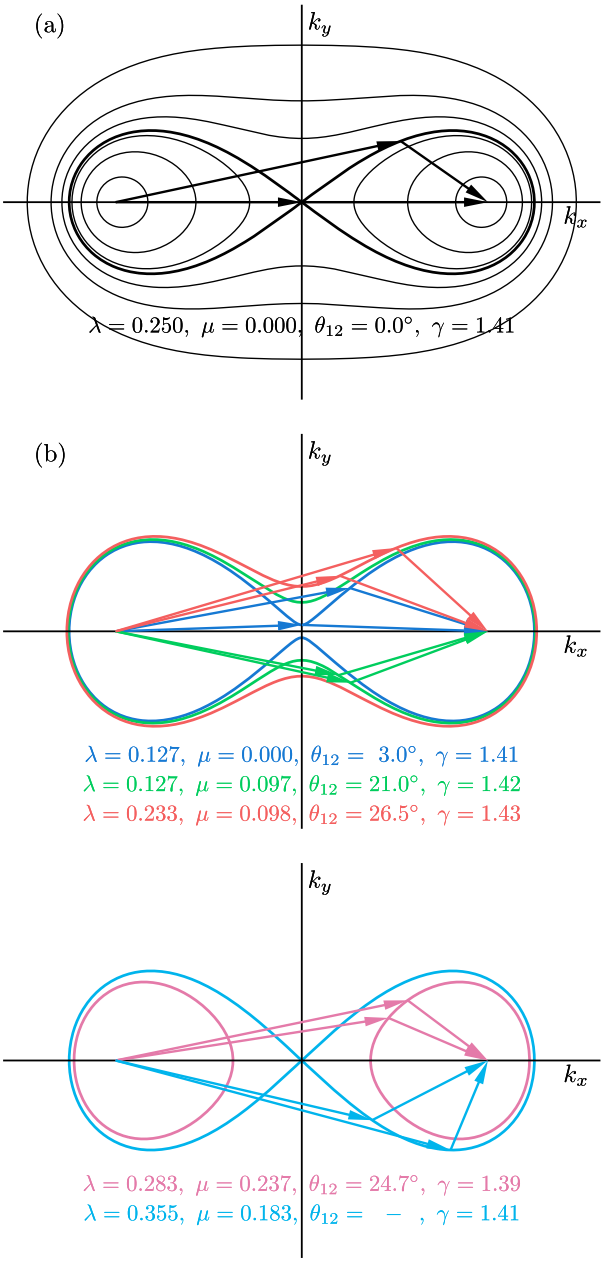

FIG. 1. Interaction diagram for $\mathbf{k}_1 + \mathbf{k}_2 = \mathbf{k}_3 + \mathbf{k}_4 = \mathbf{k}$ [after Hasselmann (1963)] with solid lines for contours of $\gamma = (\sqrt{k_1} + \sqrt{k_2})/\sqrt{\|\mathbf{k}\|}$ and vectors for quadruplet layouts: (a) the DIA quadruplet and (b) the five GMD quadruplets as specified in Table 1. For the given values of (λ, μ, θ_{12}), only one solution of (15) is shown for the clarity of this figure.

3. Model calibrations

Herein ST6 is applied with different parameterizations of S_{nl}. To distinguish these model configurations, we will refer to ST6 + DIA as ST6^D, ST6 + GMD as ST6^G, and ST6 + WRT as ST6^W. When necessary, the combination of the ST4 source terms (Ardhuin et al. 2010) and DIA (hereafter ST4^D), which is used for the operational forecasting in NOAA's National Centers for Environmental Prediction (NCEP; Alves et al. 2015), is also included for comparisons. The wind growth parameter $\beta_{\max}$ of ST4^D used is 1.33 (Ardhuin et al. 2010; Rascle and Ardhuin 2013), unless otherwise specified.

a. Calibration of ST6^D

As mentioned in section 1, our (re)calibration of ST6^D is conducted by increasing the (positive) wind input term slightly, and then finding the new tunable parameters existing in the wave breaking and swell decay terms (i.e., a_0, a_1, a_2, B_1). The amplification of S_{in} is achieved by setting $U_s \simeq \Upsilon u_* = 32 u_*$, as compared with $\Upsilon = 28$ in (7). It was found by coauthor W. Erick Rogers (2014, unpublished work) that using $\Upsilon = 32$ could improve model skills in estimating tail level in the ST6 implementation in SWAN [see also Rogers (2017)]. RBW12 calibrated a_1 and a_2 [see (9) and (10)] by using a

[4] The G35d configuration in Tolman (2013).

single-grid-point, duration-limited simulation. Because of the scarcity of observations in such idealized cases, the authors had to adopt growth curves simulated by other widely used packages (Komen et al. 1984; Rogers et al. 2003) as references. Unlike RBW12, here we decided to tune the model with fetch-limited simulations, particularly considering the extensive field studies of fetch-limited wind wave spectra (e.g., Hasselmann et al. 1973; Kahma and Calkoen 1992; Babanin and Soloviev 1998a; Romero and Melville 2010a, hereafter RM10).

For tuning purposes, we utilized a fetch-limited test under a homogeneous wind forcing with $U_{10} = 20\ \mathrm{m\,s^{-1}}$, blowing perpendicularly to a straight shoreline. Similar to Tolman and Chalikov (1996), we employed three 40-point grids with different spatial resolutions ($\Delta x =$ 2.5, 25, and 250 km, respectively) to guarantee a wide range of fetches. The spectral grid was discretized as $\Delta f/f = 0.07$ and $\Delta\theta = 10°$, with $f_0 \in [0.037, 1.027]$ Hz, $i = 1, \ldots, 50$. The fetch law for stable stratification, as suggested by Kahma and Calkoen (1992, hereafter KC92) (see also Komen et al. 1994, p. 181), was selected as the tuning reference:

$$\begin{cases} \varepsilon_* = \dfrac{H_s^2 g^2}{16 u_*^4} = 2.1 \times 10^{-3} \chi_*^{0.79} \\ \nu_* = \dfrac{f_p u_*}{g} = 2.3 \chi_*^{-0.25} / 2\pi \end{cases}, \tag{16}$$

where $\chi_* = gX/u_*^2$, X is the fetch, and f_p is the peak frequency. It is interesting to note that the fetch law from Babanin and Soloviev (1998a) is remarkably consistent with (16), except for ν_* at short fetches (Fig. 2). The power law suggested by RM10 is also in excellent agreement with the former two studies, particularly for the dimensionless energy ε_*.

We first made an attempt to determine (a_1, a_2) for ST6^D by the following subjective, loose rules:

1) ST6^D-simulated dimensionless energy ε_* and peak frequency ν_* should match the KC92 growth curves in (16) reasonably well. Specifically, $b_n^{\varepsilon *} \geq 0$, $\epsilon_n^{\varepsilon *} \leq$ 40%, and $\epsilon_n^{\nu *} \leq 10\%$, where b_n and ϵ_n are the normalized bias and root-mean-square error (RMSE; appendix A). The positiveness of $b_n^{\varepsilon *}$ is imposed due to the exclusion of the negative S_{in} and S_{swl} terms at this stage (i.e., $a_0 = B_1 = 0$).[5]

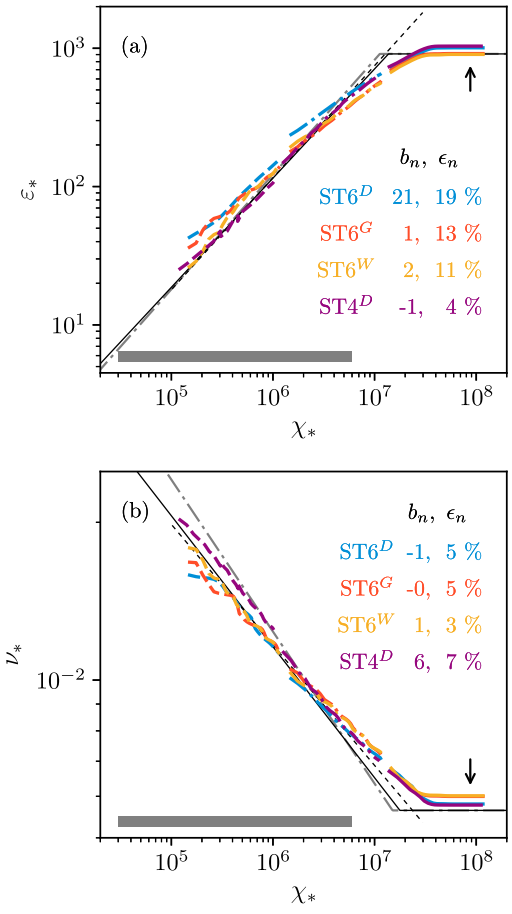

FIG. 2. (a) Dimensionless energy $\varepsilon_* = H_s^2 g^2/16u_*^4$ and (b) peak frequency $\nu_* = f_p u_*/g$ as a function of dimensionless fetch $\chi_* = gX/u_*^2$. The solid black lines represent the KC92 growth curves [(16)] and the Pierson–Moskowitz asymptotic limits [(17)]. The gray dash-dotted lines and black dotted lines are growth curves from Babanin and Soloviev (1998a) and Romero and Melville (2010a), respectively. Results from different model configurations (1D runs; see section 3c) after a 72-h model run are color-coded by blue for ST6^D, red for ST6^G, yellow for ST6^W, and purple for ST4^D. The corresponding overall error metrics (normalized bias b_n and RMSE ϵ_n; see appendix A) are also printed. Only model points within the valid range of KC92 growth curves (highlighted by the thick gray horizontal lines) were included in error analyses. Besides, the first five points of each grid were abandoned to reduce the effects of numerical errors (Tolman 1992). The dashed, dash-dotted, and solid colored lines denote points from grids with the resolution of $\Delta x = 2.5$, 25, and 250 km, respectively. The black arrows indicate the point where $X = 7500$ km, which was chosen to compute $\int T_2\, df / \int (T_1 + T_2)\, df$ for fully developed waves. Note that the negative S_{in} and S_{swl} are activated here.

2) For *fully developed* waves, for example, waves at the 30th point of the coarsest grid where $X = 7500$ km (black arrows in Fig. 2), the two-phase wave breaking term S_{ds} in (8) should satisfy $75\% \leq \int T_2\, df / \int (T_1 + T_2)\, df \leq 80\%$ (RBW12).

[5] According to our tuning exercises, $\epsilon_n^{\nu *}$ is remarkably less sensitive to the swell dissipation (i.e., negative S_{in} and S_{swl}) than $\epsilon_n^{\varepsilon *}$. Such swell-related dissipation terms may result in ~10% differences in $\epsilon_n^{\varepsilon *}$. Therefore, the criterion for $\epsilon_n^{\varepsilon *}$ was only loosely imposed (e.g., $\epsilon_n^{\varepsilon *} \leq 40\%$).

TABLE 1. Parameter setting for ST6^D, ST6^G, and ST6^W, including five parameters (Υ, a_0, a_1, a_2, B_1) from the ST6 source terms (S_{in}, S_{ds}, S_{swl}), and four parameters (λ, μ, θ_{12}, C_q) pertaining to the DIA-like (i.e., DIA and GMD) parameterizations of S_{nl}, where C_q is a proportionality constant [C in Hasselmann et al. (1985) and C_{deep} in Tolman (2013)].

	Υ	a_0	a_1	a_2	B_1	λ	μ	$\theta_{12}(^\circ)$	C_q
ST6^D	32.0	0.09	4.75×10^{-6}	7.00×10^{-5}	4.10×10^{-3}	0.25	—	—	3.00×10^{7}
ST6^G	32.0	0.05	4.75×10^{-6}	7.00×10^{-5}	6.00×10^{-3}	0.127	0.000	3.0	4.88×10^{7}
						0.127	0.097	21.0	1.26×10^{8}
						0.233	0.098	26.5	6.20×10^{7}
						0.283	0.237	24.7	2.83×10^{7}
						0.355	0.183	—[a]	1.17×10^{7}
ST6^W	32.0	0.05	4.75×10^{-6}	7.00×10^{-5}	6.00×10^{-3}	—	—	—	—

[a] For the fifth quadruplet layout of GMD (light blue arrows in Fig. 1), the three-parameter (λ, μ, θ_{12}) definition [(15)] degrades to a two-parameter (λ, μ) form, and θ_{12} is implied by the value of μ (Tolman 2013). Accordingly, a combination of ST6^G and the conservative nonlinear high-frequency filter of Tolman (2011) might be necessary to stabilize the model integration, particularly for high-resolution spectral grid (say, $\Delta\theta \le 5^\circ$).

Through our tuning exercises, we found that the two restrictions described above yield a narrow corridor in the (a_1, a_2) parameter space [see section 1 of the supplemental online material (SOM)]. To further refine these two parameters, we added another important supplementary constraint (rule 3, below).

3) For a realistic 75-day wave hindcast in Lake Michigan,[6] ST6^D should predict both H_s and mean square slope $\langle s^2 \rangle$ quite accurately (e.g., the RMSE ϵ of H_s and $\langle s^2 \rangle$ are less than 0.2 m and 10^{-3}, respectively), as compared with measurements from a single buoy 45007 (see section 2 of the SOM).

Waves prevailing in Lake Michigan are generally young and free of wind-swell interactions (Rogers and van Vledder 2013). Accordingly, the deactivation of S_{swl} and negative S_{in} in this hindcast experiment is still physically sound.

After the *optimal* (a_1, a_2) for ST6^D was established by the above-mentioned approach ($a_1 = 4.75 \times 10^{-6}$, $a_2 = 7.00 \times 10^{-5}$; Table 1), we continued the calibration of the negative wind input parameter a_0 in (6) and the swell decay coefficient B_1 in (12). Following ZBRY15, these two parameters were determined through a global hindcast of the year 2013, using a coarse longitude–latitude grid (1.25° × 1.0°) forced by winds from the NCEP Climate Forecast System version 2 (hereafter CFSv2; Saha et al. 2014).[7] By comparing with measurements from the cross-calibrated altimeter dataset produced by Young et al. (2017), we found that ST6^D with $a_0 = 0.09$ and $B_1 = 4.10 \times 10^{-3}$ (Table 1) provided acceptable skills in specification of H_s in global basins (section 3 of the SOM; bias $b = 0.03$ m and RMSE $\epsilon = 0.39$ m). Thus far, this finalizes the entire calibration procedure of ST6^D.

Figure 2 shows the ST6^D-simulated dimensionless energy ε_* and peak frequency ν_* as a function of dimensionless fetch χ_* in the fetch-limited test under $U_{10} = 20\,\mathrm{m\,s^{-1}}$. In general, wave parameters given by ST6^D are in reasonable agreement with KC92 curves in (16), as forced in our tuning process. Within the valid range of the fetch-limited observations from KC92 ($3 \times 10^4 \le \chi_* \le 6 \times 10^6$; see Komen et al. 1994, p. 180, RM10),[8] the overall ϵ_n of ε_* and ν_* are 19% and 5%, respectively. At short and intermediate fetches (e.g., $\chi_* < 6 \times 10^6$), ST6^D overestimates ε_* moderately with an overall b_n of 21%. At extremely long fetches, ST6^D agrees quite well with the Pierson–Moskowitz (PM) asymptotic limits, given by

$$\begin{cases} \varepsilon_*^{PM} = \varepsilon_{10}^{PM}/C_d^2\big|_{U_{10}=20\ \mathrm{m\ s^{-1}}} = 0.91 \times 10^3 \\ \nu_*^{PM} = \nu_{10}^{PM}\sqrt{C_d}\Big|_{U_{10}=20\ \mathrm{m\ s^{-1}}} = 5.64 \times 10^{-3}, \end{cases} \tag{17}$$

where ε_{10}^{PM} and ν_{10}^{PM} are the U_{10}-scaled PM limits from Alves et al. [2003, their (17)] and C_d is the wind-dependent drag coefficient. Here we took $C_d = 2.1 \times 10^{-3}$ for $U_{10} = 20\,\mathrm{m\,s^{-1}}$ by following the drag law described in Hwang (2011), which is also the drag law utilized by ST6 to estimate u_* (RBW12). In this case ST4^D presents an improved accuracy for ε_* ($\epsilon_n^{\varepsilon_*} = 4\%$) and a slightly degraded accuracy for ν_* ($\epsilon_n^{\nu_*} = 7\%$). The fully developed sea states reached by ST4^D

[6] The model attributes are detailed in Rogers and Wang (2007) and ZBRY15.

[7] Data sourced from NCAR's Research Data Archive (https://rda.ucar.edu/datasets/ds094.0).

[8] Komen et al. (1994, p. 180) shows that the valid range of the KC92 fetch-limited measurements is $\chi_* \in [3 \times 10^4, 4 \times 10^6]$. According to Romero and Melville (2010a, their Figs. 7c,d), the upper limit of the valid range can be safely extended to $\chi_* = 6 \times 10^6$.

are very close to those for ST6^D ($\varepsilon_* \simeq 1.00\times10^3$, $\nu_* \simeq 5.8\times10^{-3}$).

b. Calibration of ST6^G

For the GMD parameterization of $S_{\rm nl}$ with five quadruplets and a three-parameter (λ, μ, θ_{12}) quadruplet definition [(15)], there are a total of 20 free parameters to be determined.[9] Tolman and Grumbine (2013) designed a holistic genetic optimization (GO) technique to efficiently optimize these parameters altogether. The five quadruplet layouts,[10] yielded by the GO algorithm specifically for the ST6 package, are presented in Table 1 and Fig. 1. For idealized test cases selected in Tolman and Grumbine (2013) and relative to the WRT, such a GMD configuration reduces errors of the DIA by more than 50% (section 4 of the SOM), consistent with the findings in Tolman (2013).

Using the same (a_1, a_2) from ST6^D, ST6^G shows approximately 20% lower ε_* and 1% higher ν_* with slightly improved $\epsilon_n^{\varepsilon*}$ (13%) and unchanged $\epsilon_n^{\nu*}$ (5%) in the fetch-limited test (Fig. 2). The overestimation of ε_* at intermediate fetches by ST6^D is noticeably improved by ST6^G. Considering that all three tuning rules described in the previous section are still well satisfied, we decided not to adjust (a_1, a_2) for ST6^G.[11] By contrast, the global hindcast experiment for 2013 suggested an update of (a_0, B_1) to (0.05, 6.00×10^{-3}) in ST6^G (Table 1) is useful to further enhance model accuracy of H_s (section 3 of the SOM).

Since it is extremely expensive, if not impossible, to run ST6^W in realistic large-scale applications, we did not try a further calibration of ST6^W. For simplicity, ST6^W directly inherits all the parameters (i.e., a_0, a_1, a_2, B_1) from ST6^G, as shown in Table 1. Examination of Fig. 2 demonstrates that ST6^W conforms very well to ST6^G, except at short fetches ($\chi_* < 4\times10^5$). Among the three ST6 model configurations, ST6^W produces the lowest errors with $\epsilon_n^{\varepsilon*} = 11\%$ and $\epsilon_n^{\nu*} = 3\%$. The asymptotic values for ν_* from ST6^G and ST6^W are slightly higher than the value suggested by Alves et al. (2003) (6.00×10^{-3} vs 5.64×10^{-3}).

c. Fetch geometry

The last topic we would like to discuss in this section is the effect of fetch geometry on wave growth (Young 1999, p. 109). Field studies (Pettersson and Kahma 2005; Ataktürk and Katsaros 1999) suggested that for the same dimensionless fetch χ, the dimensionless energy ε values of mature waves were remarkably lower for the narrow fetch than for the broad fetch. The dimensionless frequency ν was also affected to some extent, but was clearly less sensitive than ε. It was believed that the narrow geometry constrained the development of waves propagating along directions oblique to the long axis of narrow fetches (bays or lakes). As demonstrated in Rogers and Wang (2006, their Fig. 15) and Ataktürk and Katsaros (1999, p. 643), the third-generation wave models are able to provide qualitatively consistent behavior. An interesting detail, which we think is worth mentioning and which we found from our simulations, is that the DIA-based results are more sensitive to the fetch geometry than those from the GMD and WRT.

Figure 3 presents the fetch-limited results from the one-dimensional (1D) run (i.e., the propagation of wave energy along the y direction was switched off, and the model domain became essentially infinitely wide) and the two-dimensional (2D) run (i.e., wave energy was allowed to propagate along y direction) with an aspect ratio $\mathscr{A}_r = x/y = 2$, where x and y are the length and width of the model domain, respectively. Clearly, the fully developed asymptotic energy ε_* (frequency ν_*) is lower (higher) in the 2D run (gray dotted lines in Fig. 3) due to the narrow geometry of the fetch. The differences between these asymptotic values can be quantified by

$$\mathscr{R}_q = |(q_2 - q_1)/q_1|, \tag{18}$$

where q_1 and q_2 are the asymptotic values from the 1D (broad fetch) and 2D (narrow fetch) cases. For $\mathscr{A}_r = 2$, the DIA-based models (ST6^D and ST4^D) show $\mathscr{R}_{\varepsilon*} \sim 10\%$ and $\mathscr{R}_{\nu*} = 2\%$, whereas these metrics for ST6^G and ST6^W are markedly lower ($\mathscr{R}_{\varepsilon*} \sim 5\%$ and $\mathscr{R}_{\nu*} \le 1\%$) (Table 2). Results for 2D runs with higher aspect ratios ($\mathscr{A}_r = 5,\ 10$; i.e., narrower fetches) present similar features (Table 2). The wave spectrum from the DIA is generally too broad (e.g., Hasselmann et al. 1985; Young et al. 1987) and thus becomes more constrained by the narrowness of the fetch, explaining the results we obtained here. An intuitive indication of these results is

[9] For each quadruplet, a proportionality constant C_q, which controls the magnitude of interactive contributions for this given quadruplet [$C_{\rm deep}$ in Tolman 2013, his (24)], is also freely tunable in the GMD parameterization.

[10] This GMD configuration, different from the G35d configuration in Tolman (2013, his Table 2), is specifically optimized for ST6. The optimization experiments should be repeated for other source term packages (see Tolman 2013, and section 4 of our SOM).

[11] It, however, may be worth mentioning that in the Lake Michigan hindcast, ST6^G produces somewhat inferior skills to those for ST6^D in specification of H_s and wave periods (Table S1 of the SOM). Similarly, Rogers and van Vledder (2013) also reported that the DIA-based model runs perform better for these two wave parameters than the WRT-based runs in their Lake Michigan simulations.

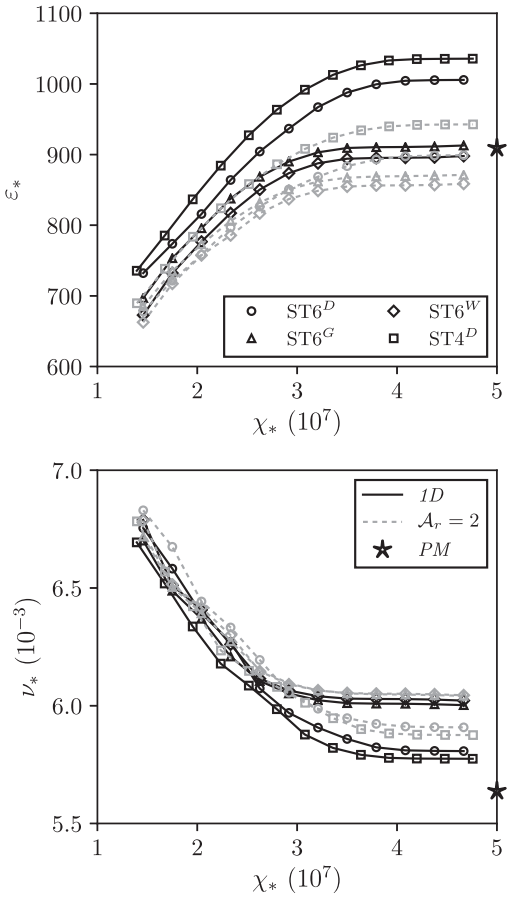

FIG. 3. Fetch-limited simulations from the third grid only ($N_x = 40$, $\Delta x = 250$ km $\rightarrow x = 10\,000$ km). The black solid lines with markers show the 1D (broad fetch) model results (i.e., the propagation of the wave energy along the y direction is turned off), the gray dashed lines with markers represent 2D (narrow fetch) model results (i.e., wave energy is allowed to propagate along the y direction) where the aspect ratio of the model domain is $\mathcal{A}_r = x/y = 2$. The black asterisks highlight the PM asymptotic limits [(17)].

the DIA-based models may have problems simulating mature waves in narrow bays/lakes.

4. Duration-limited wave growth

The previous section focuses on integrated wave parameters (e.g., significant wave height H_s and peak frequency f_p) only. However, as demonstrated by many previous studies (e.g., Banner and Young 1994; Alves and Banner 2003; Romero and Melville 2010b; Resio et al. 2016), high skills in predicting those bulk parameters do not necessarily guarantee high accuracies in modeled spectral shape. In this section, we will analyze simulated wave spectra in a much detailed way, mainly using spectral metrics suggested by RM10 and Resio et al. (2016). Most attention is dedicated to studying the following:

1) to what extent modeled spectra reflect measured properties of ocean waves, and
2) how well the GMD configuration presented in the previous section represents the exact solutions of S_{nl} (i.e., WRT).

A single-grid-point, duration-limited wave growth experiment is selected here, mainly due to its computational efficiency and its reduced sensitivity to numerical errors (e.g., RBW12). The model setup is the same as the one used in fetch-limited simulations, except that the directional grid is refined from $\Delta\theta = 10°$ to $\Delta\theta = 5°$.[12] It is, however, particularly noteworthy that in the duration-limited simulations, the high-frequency spectral tail *evolves freely without any prescribed slope*.

a. Equilibrium and saturation ranges

Based on a dimensional analysis, Phillips (1958) proposed that the high-frequency range of the wave spectrum should follow a form

$$E(f) = \alpha_P g^2 (2\pi)^{-4} f^{-5}, \tag{19}$$

if the wave breaking term S_{ds} is dominant in this specific frequency range, where α_P is the so-called Phillips constant. Toba (1973) argued the role of wind stress is also essential for small scale waves, and thus $E(f)$ should be alternatively parameterized as

$$E(f) = \alpha_T u_* g (2\pi)^{-3} f^{-4}, \tag{20}$$

where α_T is known as Toba's "constant." Later, assuming all the three physical processes (S_{in}, S_{ds}, S_{nl}) are important and comparable, Phillips (1985) reached the same form as (20). With the theoretical and observational progress in ocean waves over the past several decades (Hasselmann et al. 1973; Forristall 1981; Donelan et al. 1985; Ewans and Kibblewhite 1990; KC92; Hwang and Wang 2001; Resio et al. 2004; Babanin 2010; Lenain and Melville 2017; Zakharov 2018, among others), it has been gradually recognized that the equilibrium range ($\propto f^{-4}$) and saturation range ($\propto f^{-5}$) could coexist in wave spectra, with the equilibrium range typically located between $1.5f_p$ and $3 \sim 3.5f_p$ (Donelan et al. 1985; Resio et al. 2004) and the saturation range being applicable at higher frequencies.

[12] In the ST6^G simulation, a localized nonlinear filter (Tolman 2011) was included to suppress spurious high-frequency noise in wave spectra.

TABLE 2. Relative differences between the asymptotic values of the dimensionless energy and frequency ($\mathscr{R}_{\varepsilon*}$ and $\mathscr{R}_{\nu*}$, respectively) from the 1D (broad fetch) model run and the 2D (narrow fetch) model runs with different aspect ratios (i.e., $\mathscr{A}_r = x/y = 2, 5, 10$).

	$\mathscr{A}_r = 2$		$\mathscr{A}_r = 5$		$\mathscr{A}_r = 10$	
	$\mathscr{R}_{\varepsilon*}$ (%)	$\mathscr{R}_{\nu*}$ (%)	$\mathscr{R}_{\varepsilon*}$ (%)	$\mathscr{R}_{\nu*}$ (%)	$\mathscr{R}_{\varepsilon*}$ (%)	$\mathscr{R}_{\nu*}$ (%)
ST6^D	11	2	22	4	32	8
ST6^G	5	1	10	2	18	5
ST6^W	4	0	10	1	16	2
ST4^D	9	2	19	5	29	7

Figure 4 shows the evolution in time of the modeled omnidirectional frequency spectrum $E(f)$ and saturation spectrum $B(f)$ over 48 h of duration-limited simulations, where

$$B(f) = k^3 F(k) = \frac{(2\pi)^4 f^5 E(f)}{2g^2}. \tag{21}$$

Inspection of Fig. 4 suggests that all the three ST6 models (i.e., ST6^D, ST6^G, and ST6^W in Figs. 4a,c) yield a clear transition from a power law of approximately f^{-4} to the power law of about f^{-5}. At intermediate frequencies, wave spectra from ST4^D (Fig. 4e) also follow the slope of f^{-4} very well, whereas they fail to present the saturation range $E(f) \propto f^{-5}$ at higher frequencies. Consistent with ZBRY15 (their Fig. 5), here we find ST4^D gives a high-frequency tail roughly proportional to $f^{-4.5}$. Another important result is that wave spectra from ST6^G are in excellent agreement with those from ST6^W (Fig. 4c), indicating the high accuracy of the GMD approach in reproducing exact solutions of $S_{\rm nl}$. As expected, $E(f)$ from ST6^W and ST6^G are narrower in frequency space than those from DIA-based models (Fig. 4c vs Figs. 4a,e; see also our Figs. 7 and 8).

The saturation spectra $B(f)$ from ST6^D (Fig. 4b), for different wave ages c_p/u_* (where c_p is the peak phase velocity), converge at frequencies between 0.3 and 0.6 Hz to a constant level (hereafter B_c), indicating that, for $U_{10} = 20\,\mathrm{m\,s^{-1}}$, $B(f)$ at this frequency range is practically independent of the stage of development of ocean waves. It is worth mentioning that for lower winds (e.g., $U_{10} < 15\,\mathrm{m\,s^{-1}}$), the dependence of $B(f)$ at saturation ranges on wave age c_p/u_* or wind speed U_{10} is clearly visible (Ewans and Kibblewhite 1990, their Fig. 3). RM10 found that the average of $B(f)$ over the interval of $k \in [0.75,\ 2]$ rad m^{-1} (vertical dashed lines in Figs. 4b,d,f) are $(8 \pm 2) \times 10^{-3}$ for $U_{10} > 10\,\mathrm{m\,s^{-1}}$. The value of $B(f)$ given by ST6^D over this wavenumber range is about 7×10^{-3}, falling within the measured range of RM10. It is also noteworthy that the ST6^D-favored constant level B_c of 7×10^{-3} is in excellent agreement with field measurements from Babanin and Soloviev (1998a; $B_c = 6.6 \times 10^{-3}$) and Lenain and Melville (2017; $B_c = 7 \times 10^{-3}$). ST6^G (Fig. 4d) and ST6^W show similar $B(f)$ except B_c is slightly lower ($\sim 6 \times 10^{-3}$).[13] For $f > 0.6$ Hz, $B(f)$ from ST6 models starts to increase again, which may not be impossible as pointed out by Lenain and Melville (2017). As seen from Fig. 4f, ST4^D overestimates $B(f)$ at spectral tails as a result of the deviation of $E(f)$ from the f^{-5} form.

To scrutinize the equilibrium range, we present Toba's parameter α_T in Fig. 5 as estimated from modeled spectra using

$$\alpha_T = \frac{1}{f_u - f_l} \int_{f_l}^{f_u} \frac{(2\pi)^3 E(f) f^4}{u_* g}\, df, \tag{22}$$

where f_l and f_u are the lower and upper limits of integration. For consistency with RM10, we adopted $f_l = 1.5 f_p$ and $f_u = 0.29$ Hz.[14] The values of α_T from all three ST6 models (ST6^D, ST6^G, and ST6^W) are quite close, and higher than those from RM10. Nonetheless, they are consistent with values suggested by Resio et al. (2004) for most wave ages and by Hwang et al. (2000a) for $c_p/u_* \sim 25$. For very young waves ($c_p/u_* \sim 10$), ST6-computed α_T is noticeably lower because in such cases, equilibrium ranges are fairly narrow or might not exist (see our Fig. 6 and Babanin 2010). ST4^D overpredicts α_T compared with ST6 models (ST6^D, ST6^G, and ST6^W) and the three just-mentioned field studies. But for $c_p/u_* \leq 20$, ST4^D-modeled α_T is still within the range of [0.06, 0.11] as summarized in Phillips (1985).

b. *Transition frequency*

Since ST6 models are able to produce a transition behavior from $E(f) \propto f^{-4}$ to $E(f) \propto f^{-5}$ (Fig. 4), it is interesting to check how well the transition frequency f_t given by ST6 compares with previous studies.

[13] The $B(f)$ from ST6^W is very close to that from ST6^G (see Fig. 6), and thus not shown here for the clarity of this figure.

[14] The upper limit frequency $f_u = 0.29$ Hz corresponds to the highest resolved wavenumber (0.35 rad m^{-1}) by the Airborne Topographic Mapper utilized in RM10.

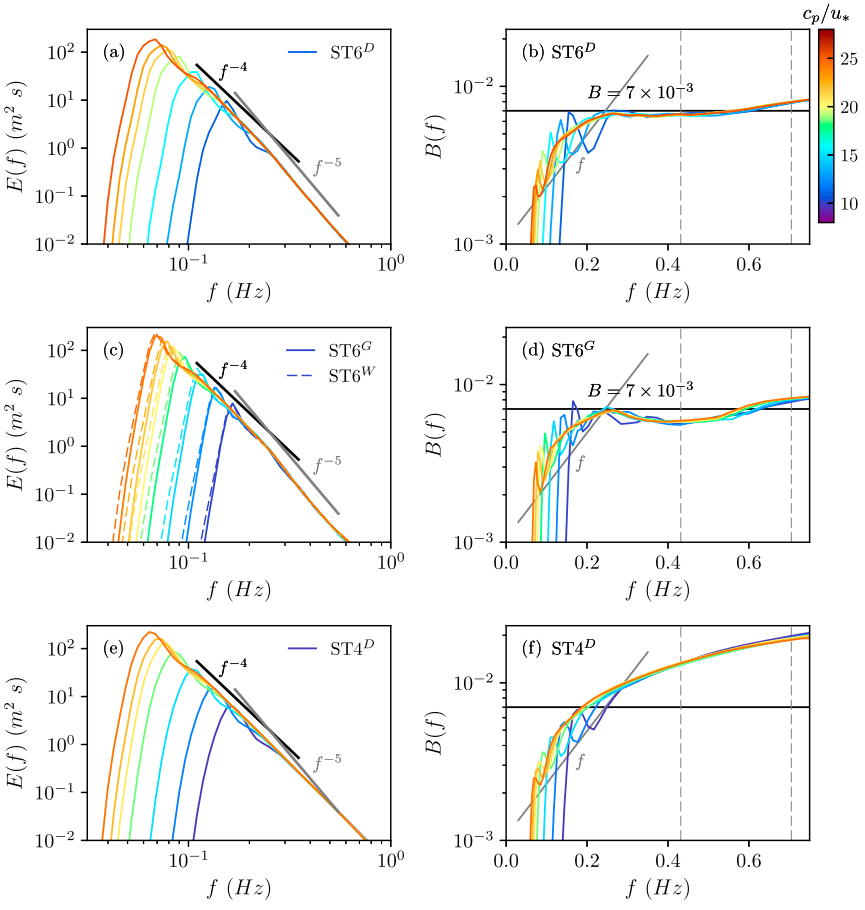

FIG. 4. The evolution of (left) omnidirectional frequency spectrum $E(f)$ and (right) saturation spectrum $B(f)$ from (a),(b) ST6^D, (c),(d) ST6^G [and ST6^W; dashed lines in (c)], and (e),(f) ST4^D. Only spectra at $t = 2$, 4, 8, 16, 24, 32, 48 h are displayed and color-coded according to the wave age c_p/u_*. In (a), (c), and (e), reference slopes proportional to f^{-4} and f^{-5} are shown as solid black and gray lines, respectively. The black lines in (b), (d), and (f) correspond to the converging constant saturation level $B = 7 \times 10^{-3}$ of field measurements from Lenain and Melville (2017), and the gray line is a reference spectral slope proportional to f.

Forristall (1981) analyzed over 4000 wave spectra measured in situ and found that f_t could be determined by

$$f_t u_*/g = 0.0275. \tag{23}$$

Based on an analysis of wave spectra collected from various wave-growth experiments, KC92 suggested that the transition from a f^{-4} to f^{-5} tail occurred at

$$2\pi f_t U_{10}/g \approx 5. \tag{24}$$

Similar to Forristall (1981), RM10 derived f_t through finding the intersection of (19) and (20):

$$2\pi f_t u_*/g = \frac{\alpha_P}{\alpha_T}, \tag{25}$$

where the authors adopted $\alpha_P = 2B = 0.016$ and $\alpha_T = 0.016(c_p/u_*)^{0.53}$ (blue line in Fig. 5). Using an alternative scaling for the equilibrium range as suggested by Resio et al. (2004),

$$E(f) = \alpha_R[(U_{10}^2 c_p)^{1/3} - u_0]g(2\pi)^{-3}f^{-4}. \tag{26}$$

Babanin (2010) quantified f_t by

$$2\pi f_t[(U_{10}^2 c_p)^{1/3} - u_0]/g = \frac{\alpha_P}{\alpha_R}, \tag{27}$$

where $\alpha_R = 6.09 \times 10^{-3}$ and $u_0 = 3.25\,\mathrm{m\,s^{-1}}$ according to Resio et al. (2004) and α_P is a wave age-dependent spectrum-tail level as proposed by Babanin and Soloviev (1998a, gray solid line in our Fig. 7a).

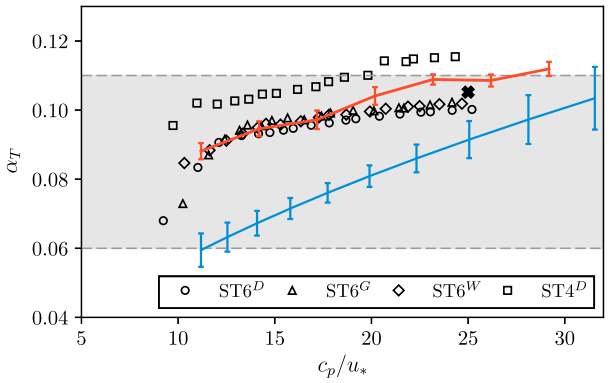

FIG. 5. Toba's parameter α_T vs the wave age c_p/u_* as simulated by ST6^D (circles), ST6^G (triangles), ST6^W (diamonds), and ST4^D (squares). The solid red and blue lines with error bars show measurements from Resio et al. (2004) and Romero and Melville (2010a). The thick × is the measurement from Hwang et al. (2000a), collected for a mature wind sea under quasi-steady winds $U_{10} = 9.5\,\mathrm{m\,s^{-1}}$. The gray shaded region indicates the range of historical measurements summarized in Phillips (1985). Figure adapted from Romero and Melville (2010a).

In Fig. 6 we replotted $B(f)$ from ST6 models against the dimensionless frequency f/f_p, together with f_t estimated from (23)–(27). As anticipated, ST6^G and ST6^W match the f^{-4} slope better than ST6^D for $1.5f_p < f < 2$–$3f_p$, particularly when $c_p/u_* > 15$. ST6^D presents a slope close to $f^{-13/3}$ at such frequency regions for those wave ages[15] (dashed line in Fig. 6a). Visual inspection of this figure suggests f_t from the ST6 models is generally compatible with Forristall's estimation. The f_t increases from below $2f_p$ for very young waves to above $4f_p$ for old wind seas; f_t from KC92 is on average $0.5\,f_p$–f_p higher. As already reported by RM10, their f_t is also higher than Forristall's values; but the difference gradually reduces as waves develop. Unlike the former three studies, Babanin (2010) favors an f_t first increases with wave age and then decreases for $c_p/u_* > 17$. This counterintuitive behavior is mainly attributed to the use of the wave age-dependent α_P (Babanin and Soloviev 1998a) in (27). During the 1990s, the form of the high-frequency wave spectrum $E(f) \propto f^n$ was in dispute (e.g., Young 1999, p. 123). Babanin and Soloviev (1998a) adopted the Joint North Sea Wave Project (JONSWAP) form (Hasselmann et al. 1973) for obtaining α_P from their field data. Unavoidably, their calculation of α_P must have included contributions

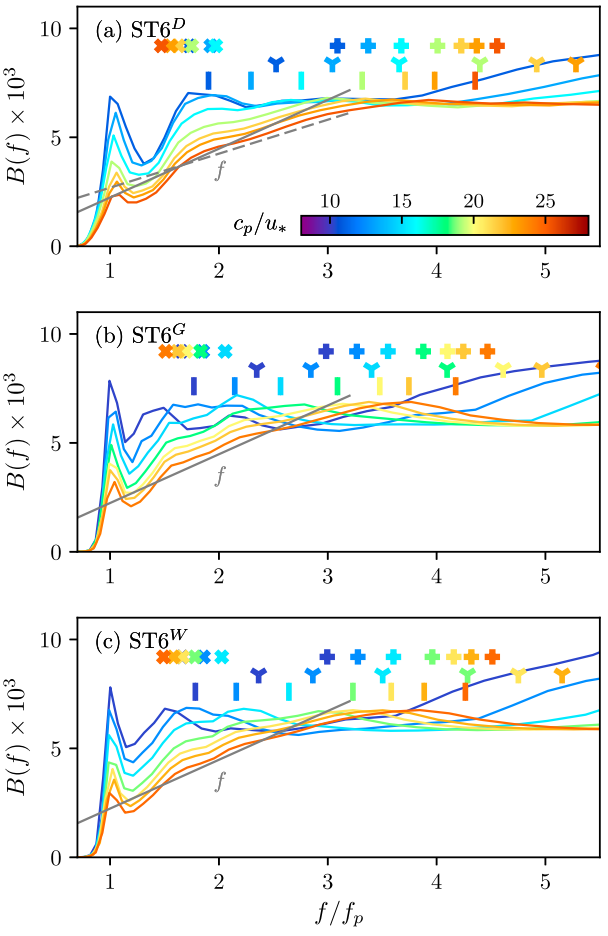

FIG. 6. As in Fig. 4, but for $B(f)$ against the dimensionless frequency f/f_p according to (a) ST6^D, (b) ST6^G, and (c) ST6^W. The color-coded markers "|", "Y", "+", and "×" highlight transition frequencies f_t for corresponding wave ages as estimated by Forristall (1981), KC92, RM10, and Babanin (2010), respectively. Note that only horizontal coordinates of these markers are meaningful. The gray solid (dashed) line highlights the reference spectral slope proportional to f ($f^{2/3}$).

from the equilibrium range, particularly for high wave ages. This is clearly demonstrated in our Fig. 7a: the modeled spectra with a nearly constant saturation level correspond to the JONSWAP spectra with an α_P value agreeing well with that from Babanin and Soloviev (1998a) (see the next subsection for more details).

c. *Spectral peakedness*

The spectral peakedness is a critical metric linked to the modulational instability of spectral waves and thus is frequently utilized in the freak wave literature (e.g., Janssen 2003; Onorato et al. 2006; Ribal et al. 2013). To examine modeled peakedness, we made an attempt to fit the generalized JONSWAP spectral form to each model

[15] The theoretical analysis in Resio et al. (2016) suggests the DIA parameterization for S_{nl} alone favors the spectral form $E(f) \sim f^{-10/3}$. The slope $f^{-13/3}$ we obtained, deviating from theirs, is probably due to the simultaneous consideration of all source terms (i.e., S_{in}, S_{nl}, S_{ds}).

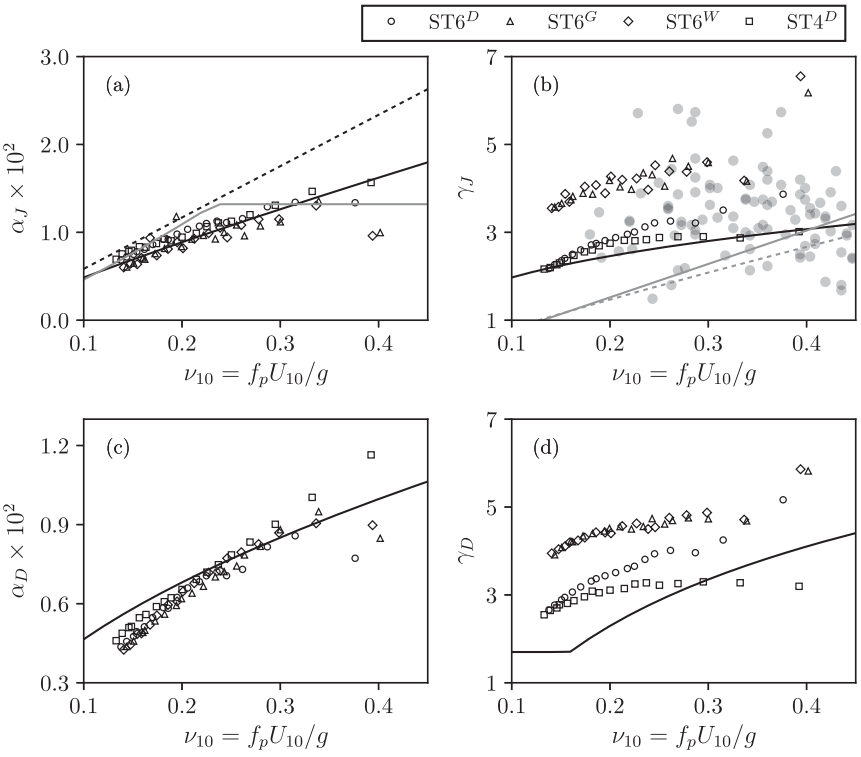

FIG. 7. The (left) high-frequency energy level α and (right) peak enhancement factor γ vs the dimensionless frequency $\nu_{10} = f_p U_{10}/g$ for wave spectra of (a),(b) the JONSWAP form ($\propto f^{-5}$) (Hasselmann et al. 1973) and (c),(d) the Donelan et al. (1985) form ($\propto f^{-4}$). The relationships in (a) and (b) are Hasselmann et al. (1976; black solid lines), Janssen [2004; black dotted line for his (2.109)], Babanin and Soloviev (1998a; gray solid lines), and Lewis and Allos (1990; gray dotted line). The gray filled circles in (b) are the JONSWAP data sourced from Young (1999, his Fig. 5.17). The dependences in (c) and (d), shown as the solid lines, are defined in Donelan et al. (1985).

spectrum. Following Young (2006), the generalized JONSWAP expression reads

$$E(f) = \alpha g^2 (2\pi)^{-4} f_p^{-(5+n)} f^n \exp\left[\frac{n}{4}\left(\frac{f}{f_p}\right)^{-4}\right] \times \gamma^{\exp[-(f-f_p)^2/2\sigma^2 f_p^2]}, \quad (28)$$

where α is the high-frequency energy level, γ is the peak enhancement factor, and σ is the peak width parameter. For $n = -5$, (28) corresponds to the JONSWAP form established by Hasselmann et al. (1973) and for $n = -4$ to the form proposed by Donelan et al. (1985).

Both of these forms of (28) with $n = -5$ and $n = -4$ were applied in the curve fitting process, and spectral parameters α and γ obtained from each of the best-fit spectra are illustrated in Fig. 7. The fit was attempted over the full-frequency range (i.e., $f_i \in [0.037, 1.027]$ Hz) with a nonlinear least squares method,[16] which minimizes the cost function $\mathscr{E} = \sum_i [E'(f_i) - E(f_i)]^2$, where $E'(f_i)$ and $E(f_i)$ denote the fitted and simulated discrete wave spectra, respectively (see also Battjes et al. 1987). For the JONSWAP form (Figs. 7a,b), the DIA-based models (ST6^D and ST4^D) yield an α marginally higher than that from ST6^G and ST6^W; α from all these four models is generally consistent with the power law proposed by Hasselmann et al. (1976) and slightly lower than power laws described in Babanin and Soloviev (1998a) and Janssen (2004). The most striking result in Fig. 7b is that γ from ST6^G and ST6^W is remarkably greater than that predicted by Hasselmann et al. (1976), Lewis and Allos (1990), and Babanin and Soloviev (1998a), although it is still within the range of values observed in JONSWAP experiment (Hasselmann et al. 1973; Young 1999); whereas ST6^D and ST4^D conform to the power law of Hasselmann et al. (1976) much better. For the form of Donelan et al. (1985) (Figs. 7c,d), α from the four models is fairly consistent and follows the dependence on wave age found by Donelan et al. (1985) reasonably well. In contrast, all

[16] The least_squares function from the scipy.optimize package.

models display a γ generally higher than that from Donelan et al. (1985). In spite of these discrepancies, the consistent features of Fig. 7 are as follows: 1) γ from ST4^D is in general the lowest, then ST6^D-simulated γ is marginally higher, and γ from ST6^G and ST6^W is the highest; and 2) except for very young waves ($\nu_{10} \sim 0.4$), both modeled α and γ decrease as the wave develops ($\nu_{10}\downarrow$), which is analogous to previous field studies (e.g., Hasselmann et al. 1976; Donelan et al. 1985; Babanin and Soloviev 1998a; Janssen 2004).

Another three metrics connected to spectral peakedness are illustrated in Fig. 8, including the spectral width F_w [ν in Babanin and Soloviev (1998a)], spectral narrowness F_n [Q_c in Rogers and van Vledder (2013)], and the Benjamin–Feir index (BFI; Janssen 2003; Onorato et al. 2006; Xiao et al. 2013):

$$F_w = \frac{m_0}{f_p E(f_p)}, \tag{29}$$

$$F_n = \frac{\max[E(f)/m_0]}{m_{-1}/m_0}, \quad \text{and} \tag{30}$$

$$\mathrm{BFI} = \frac{\sqrt{2}\delta}{2\Delta f/f_p} = \frac{k_p H_s}{2\sqrt{2}\Delta f/f_p}, \tag{31}$$

where m_n is the nth-order moment (appendix A) and Δf is the half-width at the half-maximum of $E(f)$. Remarkably, similar to what we have seen in Fig. 7, the spectral narrowness F_n (Fig. 8b) from ST6^G and ST6^W are clearly higher than that for DIA-based models (ST6^D and ST4^D), and all the models underestimate spectral width F_w from Krivinskii (1991) for most wave ages ($\nu_{10} < 0.3$; Fig. 8a). A close inspection of Fig. 8c suggests that ST6^W- and ST6^G-simulated BFI appears unrealistically high (BFI > 1).

Therefore, a consistent finding from our Figs. 7 and 8 is that the WRT- and GMD-based models (i.e., ST6^W and ST6^G), contrary to our expectation, noticeably overestimate the peakedness/narrowness (or alternatively, underestimate the width) of wave spectra. Being an approximation to the WRT, the DIA provides a slightly improved, but still problematic in general, estimation of the spectral peakedness due to its inherent tendency to unrealistically broaden the exact solutions in frequency space. Although counterintuitive, this finding is remarkably supported by a recent numerical study by Annenkov and Shrira (2018). The authors showed (their Figs. 6 and 11) that relative to the WRT results based on the Hasselmann kinetic equation (Hasselmann 1962), their direct numerical simulations based on the Zakharov integrodifferential equation (Zakharov 1968) predict ''considerably wider frequency spectra with much less pronounced peaks.'' Considering that the Zakharov equation is ''the primitive equation for a weakly nonlinear wave field'' and ''does not employ any statistical assumptions,'' and considering that the Hasselmann kinetic equation can be derived from the Zakharov equation ''by applying standard closure hypothesis,'' Annenkov and Shrira (2018) argued these systematic mismatches ''call for revision of the fundamentals'' of the Hasselmann kinetic equation. Besides, the poor performance of wave models in simulating the spectral peak implies a difficulty in predicting the occurrence of freak waves.

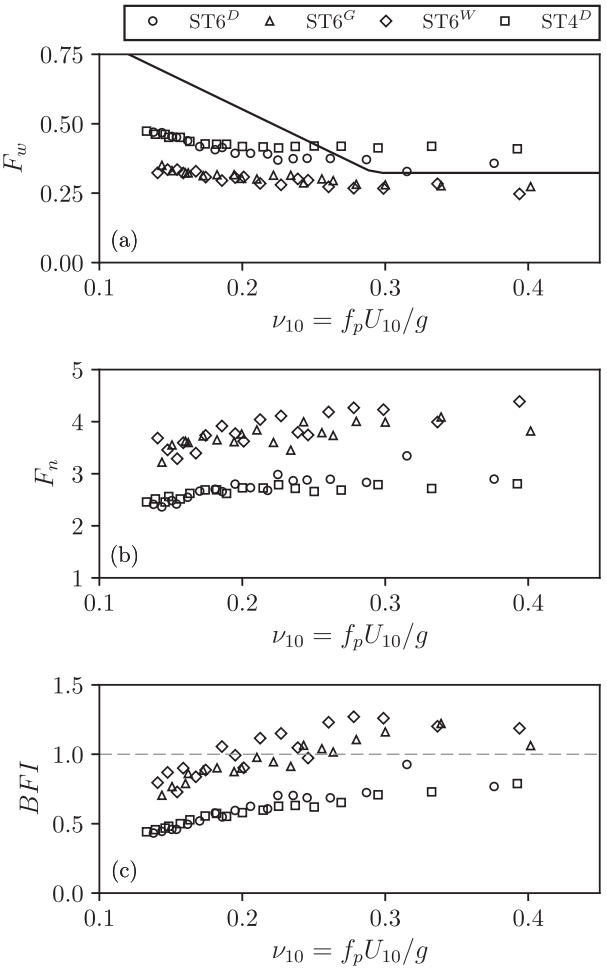

FIG. 8. The evolution of (a) spectral width F_w (Babanin and Soloviev 1998a), (b) spectral narrowness F_n (Rogers and van Vledder 2013), and (c) BFI (Onorato et al. 2006) against dimensionless frequency $\nu_{10} = f_p U_{10}/g$. The solid black line highlights the dependence of F_w on wave development suggested by Krivinskii (1991).

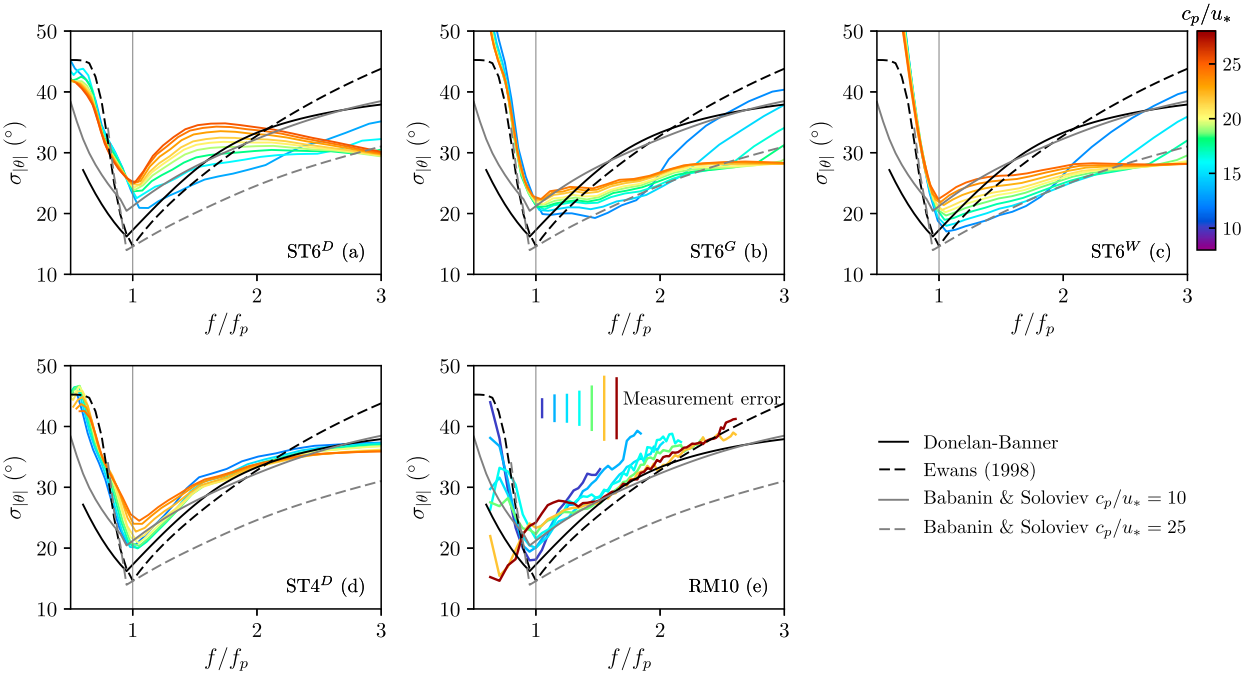

FIG. 9. Directional spreading $\sigma_{|\theta|}$ according to (a) ST6^D, (b) ST6^G, (c) ST6^W, (d) ST4^D, and (e) spatial measurements from RM10. The solid and dashed black lines illustrate $\sigma_{|\theta|}$ calculated from the directional distribution models of Donelan–Banner and Ewans (1998), respectively. The solid and dashed gray lines show $\sigma_{|\theta|}$ based on the form of Babanin and Soloviev (1998b) for $c_p/u_* = 10$ and 25, respectively. Also shown in (e) are measurement errors of peak spreading (i.e., $\sigma_{|\theta|}$ at f_p) from RM10 (vertical colored lines), starting from 3° for the lowest wave age group ($c_p/u_* \sim 10$) to 10° for the largest wave age group ($c_p/u_* \sim 28$).

d. Directional properties

The last two metrics selected in this section are associated with directional properties of wave spectra. The first metric is the directional spreading. For comparison purpose, here we adopt the definition described in RM10:

$$\sigma_{|\theta|} = \frac{\int_{-\pi/2}^{\pi/2} F(f,\vartheta)|\vartheta|\, d\vartheta}{\int_{-\pi/2}^{\pi/2} F(f,\vartheta)\, d\vartheta}, \tag{32}$$

where ϑ is the angle relative to the dominant wave direction ($\vartheta \in [-\pi, \pi]$; see, e.g., Fig. 16 of RM10).

Figure 9 illustrates $\sigma_{|\theta|}$ from different models as a function of f/f_p. Three directional distribution parameterizations are also shown as references, including 1) the unimodal $\text{sech}^2(\beta\theta)$ form proposed by Donelan et al. (1985) with the extension at high frequencies suggested by Banner (1990) (hereafter the Donelan–Banner form), where the parameter β determines the spectral spread; 2) the bimodal form as described in Ewans (1998); and 3) the same $\text{sech}^2(\beta\theta)$ form of Donelan et al. (1985) but with β suggested in Babanin and Soloviev (1998b) (hereafter the Babanin–Soloviev form). Note that unlike the former two forms, the latter form depends on the stage of wave development. Nonetheless, all these forms correspond to a $\sigma_{|\theta|}$ that is a minimum in the neighborhood of the spectral peak and then increasing toward lower and higher frequencies. Among the four wave models, ST4^D (Fig. 9d) compares the best with the two wave age-independent parametric forms (black lines in Fig. 9). The directional spreading estimated by ST4^D agrees well with Ewans' values below the peak, and then starts to match Donelan–Banner's prediction for higher frequencies. At f_p, ST4^D-computed wave spectra are moderately broader than measurements from Donelan et al. (1985) and Ewans (1998), but are still comparable to the spatial measurements from RM10 (Fig. 9e). On the other hand, wave spectra from ST6^D (Fig. 9a) are too broad at f_p–$1.5f_p$ and too narrow beyond $2f_p$. The overestimation of spreading near the spectral peak by ST6^D is partially reduced by ST6^G and ST6^W (Figs. 9b,c) due to their more accurate computations of S_{nl}. However, for $f > 1.5f_p$, $\sigma_{|\theta|}$ from ST6^G and ST6^W is fairly low, particularly when compared against measurements from Donelan et al. (1985), Ewans (1998), and RM10. The dependence of the peak spreading on c_p/u_* deserves special attention. Wave models and observations

from RM10 show an upward trend in $\sigma_{|\theta|}$ at $f \sim f_p$ as waves develop. This is, however, in contradiction to measurements from Babanin and Soloviev (1998b) and Donelan (2017), which suggest the peak of wave spectrum becomes narrower as c_p/u_* increases (e.g., see gray lines in Fig. 9). It should be remarked that there is relatively large uncertainty associated with the peak spreading measurements ($\sigma_{|\theta|}$ at f_p) by RM10. Their measurement error of peak spreading generally increases with wave age, and for $c_p/u_* \sim 28$, the error can be as large as 10° (Fig. 9e). Similarly, the directional spreading estimated from $F(f, \theta)$ measured by in situ wave buoys is rather sensitive to instrument or analysis noise, in particular for the peak spreading, which is generally low (Kuik et al. 1988, their Fig. 3).

The second directional metric to be evaluated here is the bimodality of wave components above the spectral peak, as reported by a number of previous studies (Young et al. 1995; Ewans 1998; Hwang et al. 2000b; Lenain and Melville 2017; RM10, among others). Following Wang and Hwang (2001), for a given $f > f_p$ the angular separation between the two local maxima of $F(f, \theta)$ is quantified by the metric θ_{lobe}:

$$\theta_{\text{lobe}}(f) = \frac{|\theta_1(f)| + |\theta_2(f)|}{2}, \tag{33}$$

where θ_1 and θ_2 are the locations of the maximum $F(f, \theta)$ on each side of the mean wave direction. With directional wave spectra measured with a heave-pitch-roll buoy, Ewans (1998) found that θ_{lobe} weakly depends on wave age, and its average over all stages of wave development[17] can be fitted by

$$\theta_{\text{lobe}} = 0.5 \exp(5.453 - 2.750 f_p/f) \tag{34}$$

for $f \geq f_p$. Similarly, RM10 also found a weak dependence of θ_{lobe} on wave age from their spatial measurements, showing that for $1.5 \leq (f/f_p)^2 \leq 6.5$

$$\begin{aligned}\theta'_{\text{lobe}} &= \theta_{\text{lobe}} \sqrt{c_p/u_*/5} \\ &= -0.736(f/f_p)^4 + 12.9(f/f_p)^2 - 8.35.\end{aligned} \tag{35}$$

Figure 10 presents θ'_{lobe} estimated from the four wave models, together with measurements from Ewans (1998) and RM10. For low wave ages, ST6^D (Fig. 10a) is able to exhibit a bimodal structure, although θ'_{lobe} is around 7° lower than measurements. For high wave ages, however, wave spectra from ST6^D generally lose the bimodality, as represented by $\theta'_{\text{lobe}} = 0°$. ST6^G and ST6^W (Figs. 10b,c) show enhanced ability to reproduce the bimodal behavior, except for fairly old waves ($c_p/u_* \sim 25$). ST4^D (Fig. 10d) exhibits a superior performance over ST6^D in terms of its capacity to reproduce a bimodal spectral structure. Nonetheless, it appears that the dependence of θ'_{lobe} from ST4^D on wave development is relatively stronger than those from ST6^G, ST6^W, and field measurements (Ewans 1998; RM10). The lobe ratios, defined by $r_{\text{lobe}} = [F(f, \theta_1) + F(f, \theta_2)]/2F(f, 0)$, from the four wave models are lower than values from RM10 for most of wave ages and thus are not reproduced here (section 5 of the SOM).

5. Global hindcast

After a thorough analysis of model skills in specifying the wave spectrum in academic tests, it is necessary to verify performances of ST6^D and ST6^G in realistic global hindcasts. ST6^W is excluded from the analysis here because of its computational infeasibility at the global scale.

SABZ16 conducted a comprehensive study on the comparison and assessment of different source term packages (Tolman and Chalikov 1996; Janssen 2004; Ardhuin et al. 2010; ZBRY15) available in WW3 with a global hindcast of the year 2011. For easy intercomparison with other packages evaluated in SABZ16, we selected the same year (2011) in our simulations. The global model domain is bounded within 78°S–78°N, with a resolution of 1/2° × 1/2°. The resolution of the spectral grid is $\Delta f/f = 0.1$ and $\Delta\theta = 10°$ with frequencies ranging from 0.037 to 0.953 Hz. As for SABZ16, we used winds from CFSv2 (Saha et al. 2014) as the external forcing (~0.2°; 3 hourly), and $\beta_{\max} = 1.25$ for ST4^D. It was shown that the CFSv2 winds of 2011 agreed well with altimeter U_{10} observations (SABZ16, their Fig. 2), with $b_n \sim 2\%$ and $\rho = 0.93$. (The corresponding spatial distribution of the errors of CFSv2 winds is presented in Fig. B1 in appendix B.)

a. Comparison against altimeters

Figure 11 presents comparisons of the simulated wave height H_s by different wave models and altimeter measurements from Young et al. (2017). Records of H_s from four altimeters, including *Jason-1/2*, *Envisat*, and *CryoSat-2*, were sourced, leading to a large set of model–altimeter collocations [$\mathcal{O}(10^6)$]. Relative to altimeter observations, the overall bias b and RMSE

[17] The measurements from Ewans (1998) had U_{10} in between 4.6 and 18.3 m s^{-1}, and inverse wave ages ranging from 0.7 to 1.4. Taking the average U_{10} as 12 m s^{-1}, the mean wave age c_p/u_* of his measurements corresponds to approximately 25.

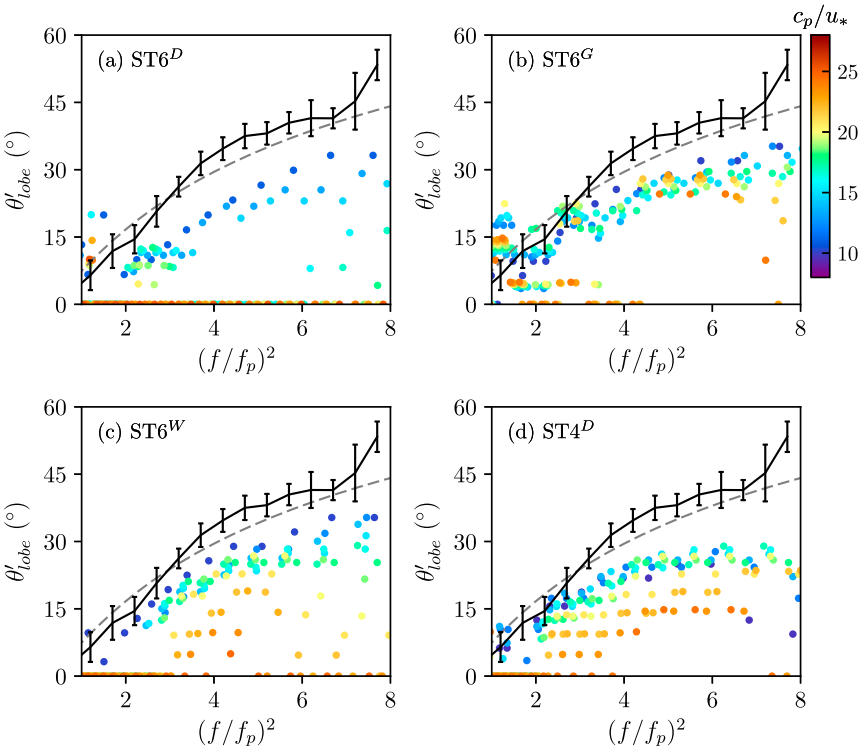

FIG. 10. The θ_{lobe}, scaled with $\sqrt{c_p/u_*/5}$, against $(f/f_p)^2$ according to (a) ST6^D, (b) ST6^G, (c) ST6^W, and (d) ST4^D. The black line with error bars show measurements collected by RM10, from which (35) was fit. The dashed line is θ'_{lobe} estimated from Ewans' formula (34) with the mean wave age $c_p/u_* = 25$ of his measurements.

ϵ in ST6^D-simulated H_s (Fig. 11a) are 0.04 m and 0.39 m, respectively. The scatter index (SI) is low (0.14) and the correlation coefficient ρ is as high as 0.96. The performance of ST6^G (Fig. 11b) is slightly improved, showing a b of 0 m, reduced ϵ (0.35 m) and SI (0.13), and an elevated ρ of 0.97. ST4^D (Fig. 11c) provides a remarkably similar skill to that of ST6^G. Note that error metrics shown here are in good agreement with those from ZBRY15 (their Fig. 13), where the authors also found that ST4^D was marginally superior to ST6^D in modeling H_s for the global basin.

The spatial distributions of the normalized bias b_n and RMSE ϵ_n of simulated H_s by each of the three models are illustrated in Fig. 12. Consistent with previous studies (e.g., Ardhuin et al. 2010; ZBRY15), H_s values from all the three models (Figs. 12a,c,e) are biased low in the western Pacific Ocean, the majority of the Atlantic Ocean, and the tropical Indian Ocean, with a b_n about −5%. The underestimation of H_s becomes slightly more noticeable in the western tropical Pacific Ocean and the tropical Atlantic Ocean, particularly in the proximity of the Indonesia archipelago ($b_n < -10\%$). This could result from the bias in CFSv2 winds in equatorial zones (SABZ16; see our Fig. B1), the neglect of shoreline reflection (Ardhuin et al. 2010), and the overblocking effect of obstruction grids utilized to represent unresolved islands (Tolman 2003). In contrast, the eastern Pacific Ocean and the Southern Ocean are dominated by positive biases in H_s. In the Southern Ocean, b_n is roughly zonally distributed and increases toward the Antarctica from 5% to 25%. Ardhuin et al. (2011) demonstrated that including the blocking effect of small-size icebergs could reduce positive biases of H_s south of 50°S. All the three wave models also share a similar pattern of the normalized RMSE (Figs. 12b,d,f): ϵ_n in most of oceans is below 15%, whereas regions such as the equatorial western Pacific Ocean and the midlatitudes in the North Atlantic Ocean correspond to a moderately higher ϵ_n (~20%); ϵ_n adjacent to Antarctica is the highest, and could be above 25%. Once again, this is comparable to results from Ardhuin et al. (2010) and ZBRY15. A close inspection of Figs. 12b, 12d, and 12f suggests that ST6^G and ST4^D perform slightly better than ST6^D, analogous to what we have seen in Fig. 11.

The geophysical mismatches presented in Fig. 12 can be partially, but not fully, explained by the errors of wind forcing (Fig. B1). For example, the overestimation

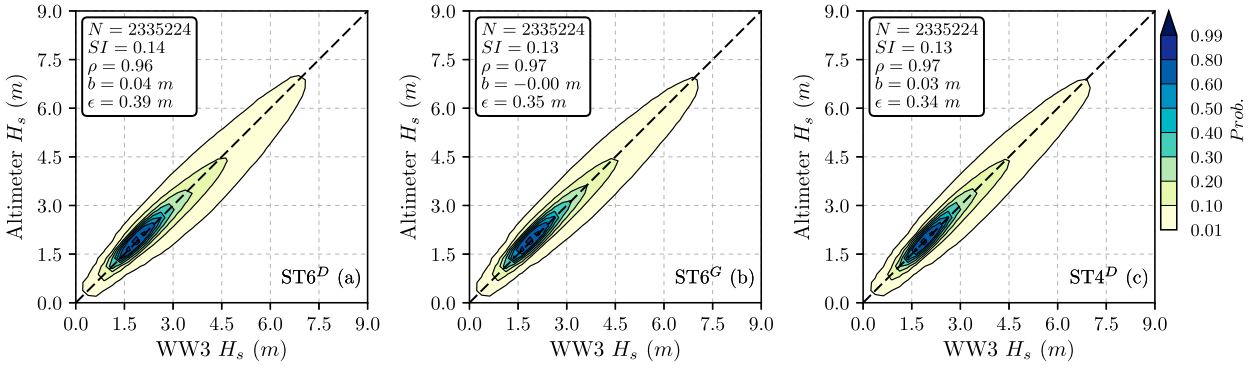

FIG. 11. Comparison of H_s for the 2011 global hindcast between altimeters and wave model (a) ST6^D, (b) ST6^G, and (c) ST4^D. The dashed line is the 1:1 line. Error metrics printed in the inset of each panel includes the total number of model–altimeter collocations N, bias b, RMSE ϵ, correlation coefficient ρ, and scatter index SI (see appendix A).

of H_s in the eastern Bay of Bengal, the western Arabian Sea, the Hudson Bay, and the Argentine Sea can be attributed to the biased-high CFSv2 wind forcing. The overall negative bias of H_s dominated in the central Pacific, Atlantic, and Indian Oceans is in line with the overall underestimation of U_{10} by CFSv2 as well. Besides, the relatively high ϵ_n of the simulated H_s present in the western midlatitude Pacific and Atlantic Oceans and the northern Indian Ocean correlates well with the comparatively high ϵ_n of U_{10}. Nonetheless, the signs of the biases of H_s and U_{10} in the eastern Pacific Ocean and the entire Southern Ocean are opposite, suggesting that other physical factors are operative. A close inspection of Fig. 12 indicates that wave energy was overestimated in the zone of the southern westerlies and then these overestimated wave energy propagates northeastward as swell to the eastern coast of the South Pacific Ocean. A detailed analysis of the wave model biases in the Southern Ocean, as done by Ardhuin et al. (2011) and Rapizo et al. (2018), is left for future studies. The reader is also referred to Ardhuin et al. (2010, p. 1930) for further discussions about the spatial distribution of wave model errors.

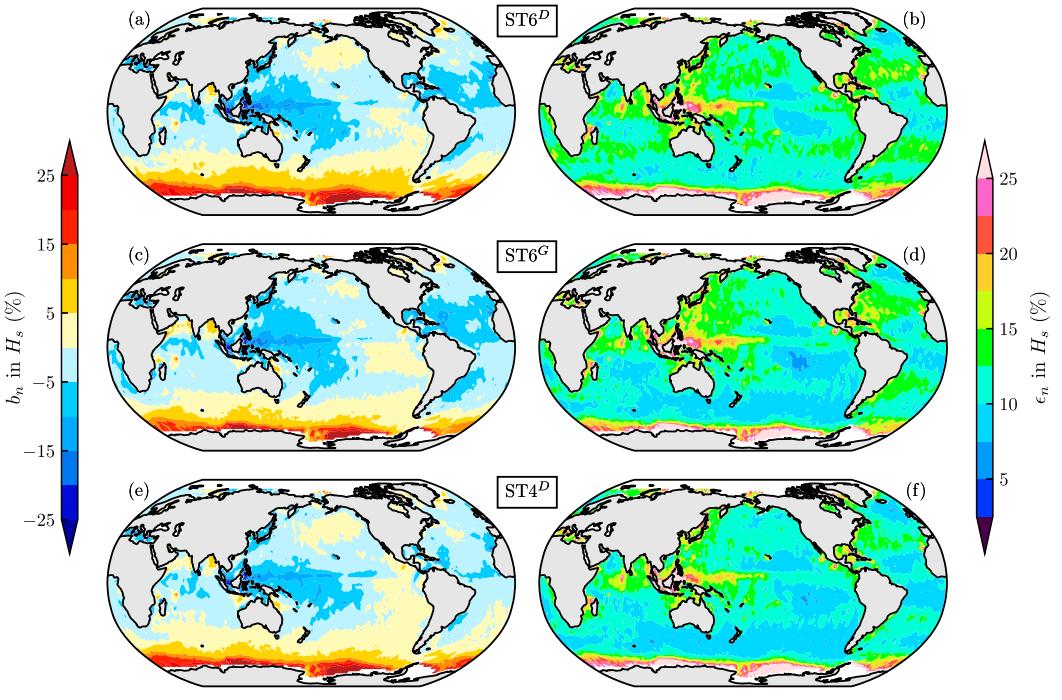

FIG. 12. Error metrics of H_s gridded in 2° × 2° bins for the 2011 global hindcast according to (a),(b) ST6^D, (c),(d) ST6^G, and (e),(f) ST4^D, showing (left) normalized bias b_n and (right) normalized RMSE ϵ_n.

b. Comparison against NDBC buoys

The validation of model simulations against in situ buoys was also conducted using observations from a total of 21 stations (Fig. 13) maintained by the U.S. National Data Buoy Center (NDBC; http://www.ndbc.noaa.gov). Closely following SABZ16, we only selected wave buoys that provide two-dimensional wave spectra and that are located in deep water (depth $d > 300$ m).

Figure 14 displays Taylor diagrams (Taylor 2001) summarizing the statistical comparison between wave models and buoys. Apart from wave parameters scrutinized by SABZ16 (e.g., wave height H_s, wave period $T_{0,2}$, mean square slope $\langle s^2 \rangle$, directional spreading σ_θ; see appendix A for definitions), we include another three complementary wave quantities, namely the wave period $T_{0,-1}$ (appendix A), the narrowness of one-dimensional spectrum F_n [(30)], and the partial significant wave height $H_{s,i}$ (Rogers and Wang 2007; Li and Holt 2009), given by

$$H_{s,i} = 4\sqrt{\int_{f_{l,i}}^{f_{u,i}} \int_0^{2\pi} F(f,\theta)\, df\, d\theta}, \tag{36}$$

where $f_{l,i}$ and $f_{h,i}$ are lower and upper integral limits. Similar to Li and Holt (2009), we divided the overlapping frequency range of buoys and models (i.e., [0.037, 0.485] Hz) into four bands with band boundaries locating at $f_{u,i} = 0.06$, 0.09, 0.20 Hz, $i = 1, 2, 3$. Based on a 10-day duration hindcast for Lake Michigan, Rogers and van Vledder (2013) clearly demonstrated that wave models using DIA for $S_{\rm nl}$ tend to overestimate energy below the spectral peak and underspecify spectral narrowness and that using WRT for $S_{\rm nl}$ instead of DIA could significantly alleviate such model biases. Therefore, examinations of $H_{s,i}$ and F_n could be beneficial to identify possible advantages of GMD over DIA. Similarly, the wave period $T_{0,-1}$ is especially relevant for the low-frequency part of the wave spectrum, and thus an evaluation of this specific period may also be informative. The Taylor diagram is not applicable to vector quantities. To give a rough idea of model skills in computing wave direction, we also plotted zonal and meridional wave heights $(H_{s,z}, H_{s,m}) = H_s(\cos\theta_w, \sin\theta_w)$, defined in a similar fashion as zonal and meridional winds $(U_{10,z}, U_{10,m}) = U_{10}(\cos\theta_u, \sin\theta_u)$, where θ_u and θ_w are wind direction and mean wave direction (appendix A), respectively. It may be also useful to mention that the mean square slope $\langle s^2 \rangle$ used here is actually a low-pass mean square slope as we are just looking at the waves in the buoy frequency range ($f < 0.485$ Hz).

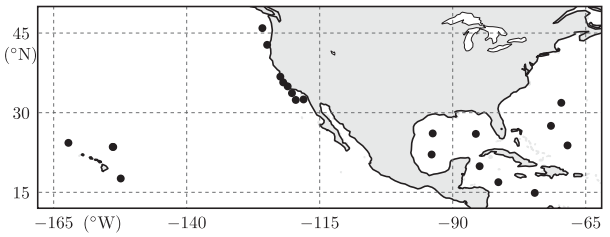

FIG. 13. A total of 21 NDBC buoys (filled circles) used in the model–buoy comparison.

Our Fig. 14 suggests that wave height H_s, wave periods $T_{0,2}$ and $T_{0,-1}$, mean square slope $\langle s^2 \rangle$, and zonal wave height $H_{s,z}$ are generally well estimated by all three wave models, corresponding to a correlation coefficient ρ greater than 0.9, a normalized standard deviation between 0.85 and 1.1, and a normalized centered RMSE ϵ_n^c less than 0.5. Overall, the simulated H_s is around 6% biased low at these selected buoy locations, consistent with the model–altimeter comparison shown in our Fig. 12. Wave energy at frequencies beyond 0.06 Hz (i.e., $H_{s,2}$, $H_{s,3}$, and $H_{s,4}$ in Fig. 14) is simulated with a remarkably high accuracy as well. Surprisingly, model skills in estimating meridional wave height $H_{s,m}$ is appreciably inferior to those for zonal wave height $H_{s,z}$, as indicated by a lower ρ and higher ϵ_n^c. By contrast, error metrics for zonal and meridional winds ($U_{10,z}$, $U_{10,m}$; see white and gray stars in Fig. 14a) are not that noticeably different. Interestingly, ST6^G indeed provides more accurate $T_{0,-1}$ ($\epsilon_n = 9\%$, $\rho = 0.94$) as compared with ST6^D ($\epsilon_n = 12\%$, $\rho = 0.92$) and ST4^D ($\epsilon_n = 11\%$, $\rho = 0.93$).

The directional spreading σ_θ and spectral narrowness F_n are the two most poorly simulated quantities. Both of these wave parameters show a ϵ_n^c within [0.8, 0.9]. The ρ of simulated σ_θ is about 0.7–0.75, and the ρ for F_n is even lower (~0.5). The variability of σ_θ is overestimated by around 20%; in contrast, models underestimate the variability of F_n more than 35%. In terms of correlation coefficient ρ, ST6^G yields a slightly improved estimation of σ_θ ($\rho = 0.75$ for ST6^G vs $\rho = 0.72$, 0.70 for ST6^D and ST4^D, respectively) and F_n ($\rho = 0.55$ for ST6^G vs $\rho = 0.48$ for ST6^D and ST4^D). The DIA is known to overpredict directional spreading of wave spectrum (see, e.g., Fig. 9a vs Figs. 9b,c). When compared with buoy observations, model spectra however turn out to be slightly too narrow, indicated by the negative b_n (−7% and −5% for ST6^D and ST4^D). As anticipated, σ_θ from ST6^G is more biased (−12%). The underestimation of spreading might be attributed to inherent errors in directional distribution of different source functions and the neglect of effects of currents on waves, as already pointed out by SABZ16.

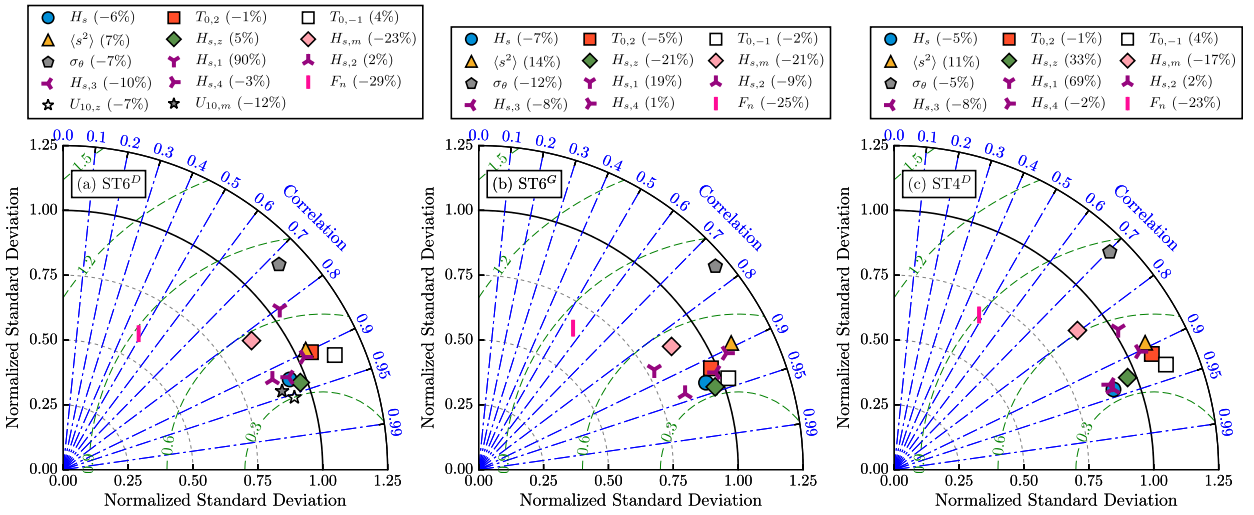

FIG. 14. Taylor diagram summarizing the statistical comparison between NDBC buoys and wave models: (a) ST6^D, (b) ST6^G, and (c) ST4^D. The wave parameters represented by different colored-markers are interpreted in figure legends. Values in parentheses identify the normalized bias b_n of each wave parameter. The last two variables $U_{10,z}$ and $U_{10,m}$ in (a), shown as white and gray stars, illustrate comparisons of zonal and meridional winds between CFSv2 and NDBC buoys.

Numerical simulations (e.g., Fan et al. 2009a,b; Komen et al. 1994, p. 359), laboratory experiments (Rapizo et al. 2016), and field observations (Romero et al. 2017) have shown that ocean currents could broaden wave spectrum due to their refraction and scattering of wave rays. A detailed analysis of the impact of ocean currents on directionality of ocean waves will be pursued in the future. In line with Rogers and van Vledder (2013), a more accurate parameterization of $S_{\rm nl}$ is helpful for reducing the negative bias in spectral narrowness F_n given by DIA ($b_n = -29\%$ for ST6^D vs $b_n = -25\%$ for ST6^G). The improvement in modeling F_n shown here, however, is considerably less than that reported in Rogers and van Vledder (2013).

The most noticeable advantage of GMD over DIA is seen in comparisons of long-period wave energy $H_{s,1}$ ($f_{u,1} = 0.06$ Hz or equivalently wave period $T > 16.6$ s). Clearly from Fig. 14, the accuracy of modeled $H_{s,1}$ is not as high as that for the three other counterparts ($H_{s,2}$, $H_{s,3}$, and $H_{s,4}$). ST6^D (Fig. 14a) exhibits a normalized bias b_n of 90% for $H_{s,1}$, indicating a serious overestimation of energy at frequencies below 0.06 Hz. ST4^D (Fig. 14c) provides a somewhat improved performance in specifying $H_{s,1}$ ($b_n = 69\%$). This large positive bias is significantly reduced in the ST6^G simulation, as corroborated by a much lower b_n (19%). The variability of $H_{s,1}$ is underestimated by ST6^G by around 20%.

To highlight improvements in simulating high-frequency energy brought about by the recalibrated ST6^D over its predecessor (ZBRY15), and improvements in modeling low-frequency energy brought about by use of the GMD over the DIA, we replotted the mean square slope $\langle s^2 \rangle$ and partial wave height $H_{s,i}$ in Figs. 15 and 16, respectively. Similar to Ardhuin et al. (2010) and SABZ16, Fig. 15 illustrates the averaged mean square slope $\langle s^2 \rangle$ over each 1 m s^{-1} bin of U_{10} and each 0.5 m bin of H_s. SABZ16 (their Fig. 7) reported that the predecessor of ST6^D (ZBRY15) was inclined to overestimate $\langle s^2 \rangle$, particularly under high winds. For instance, for $U_{10} = 15$ m s^{-1} and $H_s \sim 4.5$ m, the old version of ST6^D overestimated $\langle s^2 \rangle$ by more than 30%. Similar to ST4^D (Fig. 15d), the recalibrated ST6^D and ST6^G (Figs. 15b,c) reproduce the variability of $\langle s^2 \rangle$ with U_{10} and H_s as measured by buoys (Fig. 15a) remarkably well. The scatter density plots of $H_{s,i}$ shown in Fig. 16 provide a more intuitive visualization of the decrease of model errors in calculating $H_{s,1}$ by ST6^G relative to that for the DIA-based simulations (Figs. 16a–c). All the four error metrics (i.e., b, ϵ, ρ, and SI) for $H_{s,1}$ provided by ST6^G are slightly better than those from ST6^D and ST4^D. As already mentioned, this improvement is consistent with what we expect from the findings of Rogers and van Vledder (2013). It is worth noting that the remaining marginally positive bias $b_n = 0.03$ m of $H_{s,1}$ in the ST6^G simulation can be further reduced when coastlines and small islands are resolved better, as demonstrated in Li (2012, his Fig. 5).

One detail that needs to be further clarified is that the swell decay coefficient B_1 in (12) for ST6^G is slightly higher than that used for ST6^D (6.0×10^{-3} vs 4.1×10^{-3}; Table 1). One may argue that the reduction of positive bias in $H_{s,1}$ by ST6^G might be attributed to the higher B_1. Another global hindcast of 2011 by ST6^D but using a_0 and B_1 from ST6^G (i.e., $a_1 = 0.05$ and $B_1 = 6.0 \times 10^{-3}$)

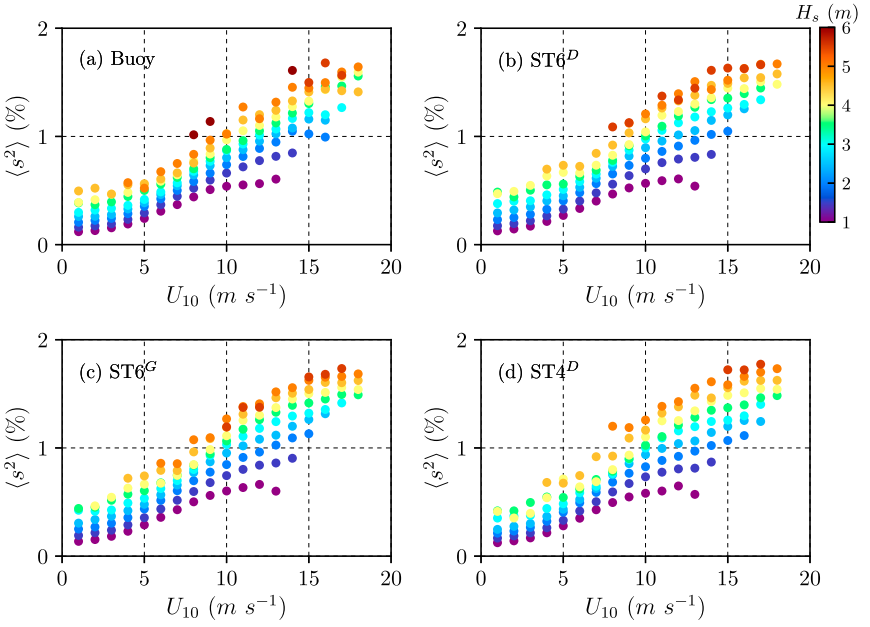

FIG. 15. Averaged mean square slope $\langle s^2 \rangle$ in each 1 m s^{-1} bin of U_{10} and each 0.5 m bin of H_s according to (a) NDBC buoys, (b) ST6^D, (c) ST6^G, and (d) ST4^D.

corresponds to a b_n in $H_{s,1}$ of 78% (section 6 of the SOM), which is still considerably higher than that for ST6^G (19%). Therefore, the advantage of ST6^G over ST6^D in estimating low-frequency wave energy is a robust feature.

Having seen the marked advantage of GMD over DIA in estimating low-frequency wave energy, we expect that GMD might also be advantageous in characterizing different wave systems, at least for low-frequency swells. This is checked in Fig. 17, where Taylor diagrams for partitioned wave parameters are displayed. The watershed algorithm (Hanson and Phillips 2001) combined with a digital filter proposed by Portilla et al. (2009) was utilized to identify distinct partitions from two-dimensional wave spectrum $F(f, \theta)$. Following Hanson and Phillips (2001), partitions with $c_p/U_{10}\cos\theta_{up} \le 1.5$ were considered as wind seas and swells otherwise, where θ_{up} is the angle between wind θ_u and partition peaks θ_p. Following Delpey et al. (2010) and SABZ16, another criterion

$$d_n = \|f_p^o \cos\theta_p^o - f_p^m \cos\theta_p^m, f_p^o \sin\theta_p^o - f_p^m \sin\theta_p^m\|/f_p^o \le 0.3 \quad (37)$$

was successively applied to match partitions from buoys and models, where d_n is the normalized Euclidean distance between the partition peak of the buoys (f_p^o, θ_p^o) and that of the models (f_p^m, θ_p^m). More than 130 000 matchups are located between buoys and each of three wave models, among which the proportion of wind seas is strikingly low (~18%). This is, however, comparable to the frequency of occurrence of pure wind sea at buoy locations as presented in Hanley et al. (2010, their Fig. 9). Inspection of Fig. 17 suggests that model skills in estimating wind-sea parameters (markers with outlines) are higher than those for swell, with the only exception being the peak wave period T_p. As for Fig. 14, the directional spreading σ_θ and spectral narrowness F_n are the most poorly resolved quantities. The wave models have no skills for σ_θ of swells. Contrary to our expectation, ST6^G (Fig. 17b) only shows marginally improved performance in representing different wave systems as compared against ST6^D and ST4^D (Figs. 17a,c; Table 3).

The last problem to be addressed here is the computational efficiency of different wave models. Table 4 shows the normalized model run times obtained with wave models using different nonlinear solvers and different prognostic frequency ranges. The high-frequency limit $f_{h,f}$ of the prognostic region of the spectrum is defined by $f_{h,f} = N_{h,f}/T_{0,-1}$ (appendix A), where $N_{h,f}$ is a real number and $N_{h,f} \ge 2.5$ is generally used in the literature (e.g., Hasselmann et al. 1988). Consistent with ZBRY15, ST4^D is about 40% more expensive than ST6^D. ST6^G is around 5.6 times as expensive as ST6^D, indicating that the GMD configuration with five quadruplets and a three-parameter quadruplet definition might not be

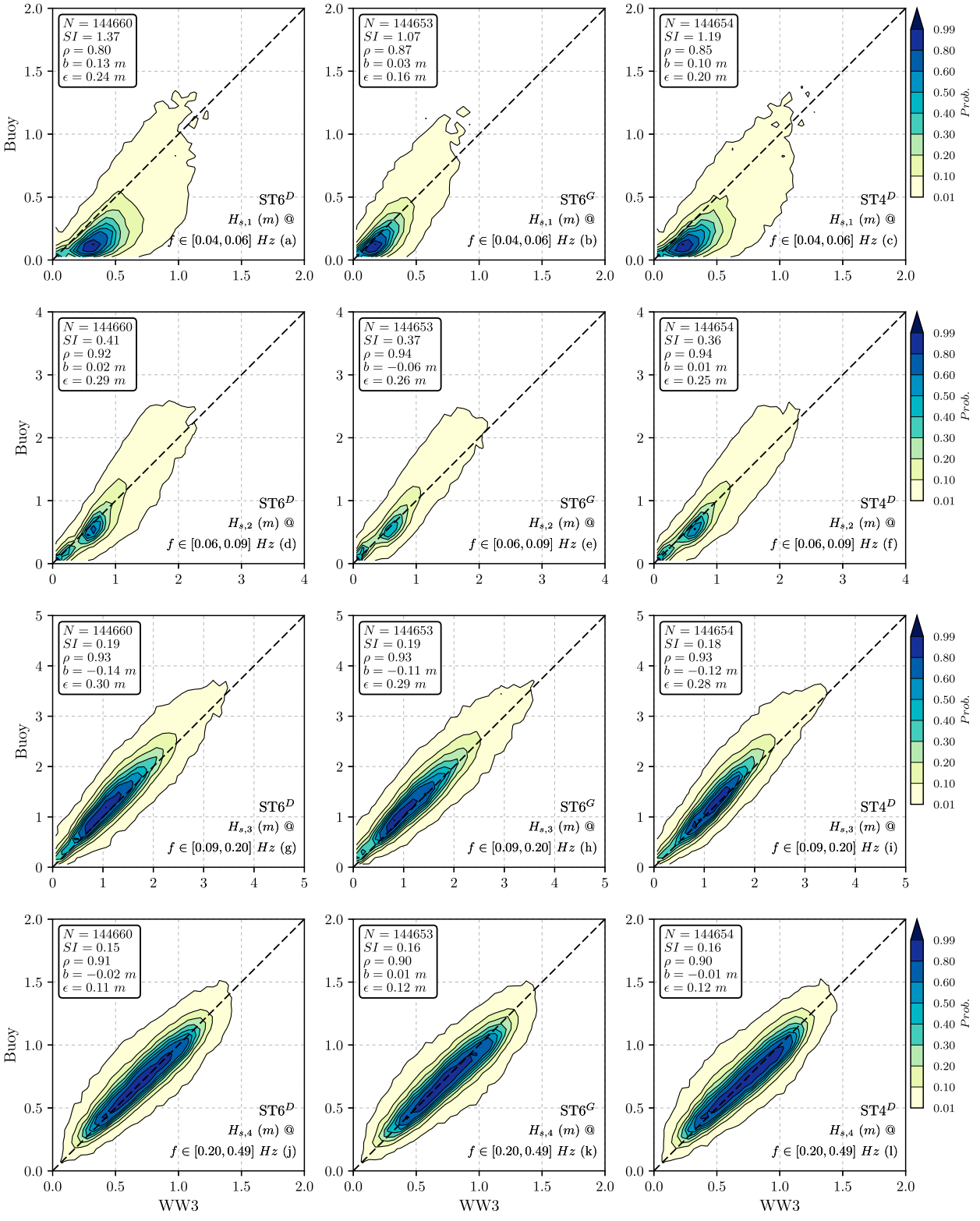

FIG. 16. Comparison of partial wave heights for (top) $H_{s,1}$, (top middle) $H_{s,2}$, (bottom middle) $H_{s,3}$, and (bottom) $H_{s,4}$ between NDBC buoys and wave models: (left) ST6^D, (center) ST6^G, and (right) ST4^D. The lower and upper limits $f_{l,i}$ and $f_{h,i}$ [(36)] are printed in the lower-right corner of each panel.

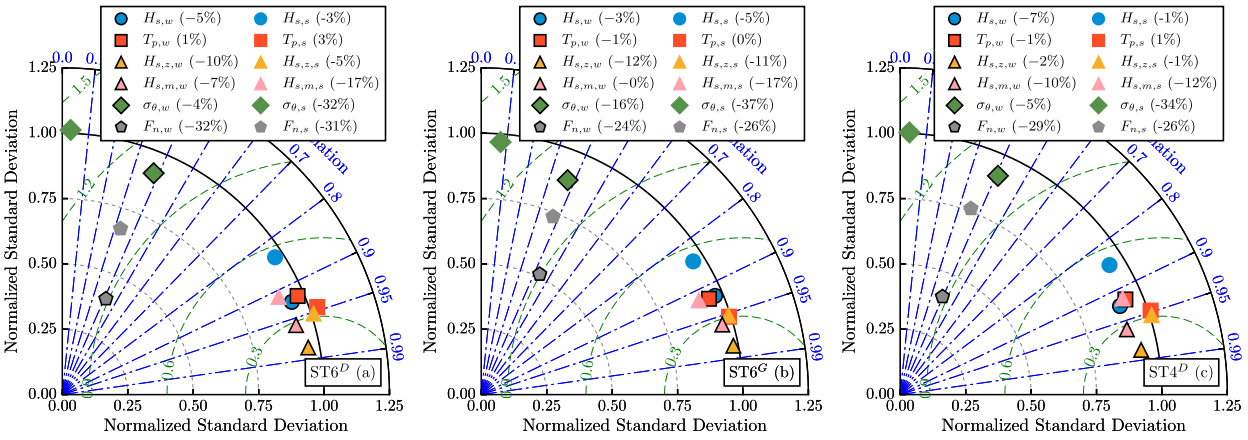

FIG. 17. As in Fig. 14, but for partitioned wave parameters from (a) ST6^D, (b) ST6^G, and (c) ST4^D. The last subscripts w and s of variables printed in figure legends denote parameters for wind sea (markers with black outlines) and swell (markers without black outlines), respectively.

economically feasible for operational purpose (see also Tolman 2013). The GMD approach with less complex configurations, as described in Tolman (2013) and Tolman and Grumbine (2013), should be pursued for operational research.

6. Concluding remarks

In this paper, the observation-based source term package in WW3, that is, the ST6 for $S_{\text{in}} + S_{\text{ds}} + S_{\text{wl}}$ (RBW12; ZBRY15), is recalibrated and verified through a series of academic and realistic simulations, including the fetch/duration-limited test, a Lake Michigan (no swell) hindcast, and a 1-yr global hindcast. In addition to the traditional bulk (integral) criteria, we introduced spectral metrics for model validations. We also specifically optimized the GMD nonlinear solver for ST6 (Fig. 1) in order to investigate the DIA-induced uncertainties in spectral wave modeling. Key findings are summarized below:

1) The updated ST6^D (i.e., ST6 + DIA) and ST6^G (i.e., ST6 + GMD) not only are skillful in simulating commonly used bulk wave parameters (e.g., H_s and wave periods) but also accurately represent the high-frequency wave spectrum [in terms of the saturation spectrum $B(f)$ and mean square slope $\langle s^2 \rangle$]. The overestimation of high-frequency wave energy by ST6's predecessor (e.g., ZBRY15) is resolved by the recalibration described here (e.g., Fig. 15).
2) In the duration-limited test, $E(f)$ simulated by ST6 models [ST6^D, ST6^G, and ST6^W (i.e., ST6 + WRT); Figs. 4a,c,e] shows a clear transition behavior from the power law of approximately f^{-4} to the power law of approximately f^{-5}. The modeled energy level of the equilibrium range [$E(f) \propto f^{-4}$], as represented by the wave age-dependent Toba's parameter α_T, is in good agreement with field measurements from Hwang et al. (2000a) and Resio et al. (2004) (Fig. 5). The saturation level $B(f)$ yielded by these three ST6 models is also consistent with observations from Babanin and Soloviev (1998a), RM10, and Lenain and Melville (2017) (Figs. 4b,d,f). In addition, the ST6-predicted transition frequency f_t from an $E(f) \propto f^{-4}$ to $E(f) \propto f^{-5}$ is comparable to buoy data from Forristall (1981).
3) The wave spectra from ST6^G are in excellent agreement with those from ST6^W, particularly in the frequency space (Figs. 4–9), illustrating the high accuracy of the GMD approach in reproducing exact solutions of S_{nl} from WRT. In the global hindcast, ST6^G exhibits a much better performance in predicting low-frequency wave energy. The normalized biases of $H_{s,1}$ (wave period $T > 16.6$ s) given by ST6^D and ST4^D are 90% and 69%, respectively, whereas such model errors are significantly reduced by ST6^G ($b_n = 19\%$) (Figs. 14 and 16), which is analogous to the findings from Rogers and van Vledder (2013). Nonetheless, contrary to our expectation, ST6^G only provides marginal improvement in characterizing different wave systems (i.e., wind sea and swell; Fig. 17). The GMD configuration used here is ~5 times more expensive than the DIA (Table 4) and therefore might not be economically feasible for operational forecasting.
4) When we fit the generalized JONSWAP spectrum (28) to the modeled $E(f)$ from the duration-limited

TABLE 3. Statistical comparison (as represented by the normalized RMSE ϵ_n and correlation coefficient ρ) of partitioned wave parameters between NDBC buoys and wave models. The normalized bias b_n is presented in Fig. 17 and thus is not reproduced here.

	$H_{s,w}$		$T_{p,w}$		$H_{s,z,w}$		$H_{s,m,w}$		$\sigma_{\theta,w}$		$F_{n,w}$	
Wind sea	ϵ_n	ρ	ϵ_n	ρ	ϵ_n	ρ	ϵ_n	ρ	ϵ_n	ρ	ϵ_n	ρ
ST6^D	0.17	0.93	0.09	0.92	0.18	0.98	0.26	0.96	0.17	0.38	0.40	0.41
ST6^G	0.17	0.92	0.10	0.92	0.19	0.98	0.25	0.96	0.23	0.37	0.35	0.44
ST4^D	0.17	0.93	0.09	0.92	0.18	0.98	0.26	0.96	0.18	0.41	0.38	0.40
	$H_{s,s}$		$T_{p,s}$		$H_{s,z,s}$		$H_{s,m,s}$		$\sigma_{\theta,s}$		$F_{n,s}$	
Swell	ϵ_n	ρ	ϵ_n	ρ	ϵ_n	ρ	ϵ_n	ρ	ϵ_n	ρ	ϵ_n	ρ
ST6^D	0.28	0.84	0.10	0.95	0.30	0.95	0.38	0.91	0.48	0.03	0.43	0.33
ST6^G	0.27	0.85	0.09	0.95	0.30	0.95	0.37	0.92	0.50	0.07	0.40	0.37
ST4^D	0.27	0.85	0.10	0.95	0.30	0.95	0.37	0.92	0.49	0.03	0.40	0.35

case, the simulated high-frequency α is generally consistent with previous field studies (e.g., Hasselmann et al. 1976; Donelan et al. 1985). The simulated spectral peakedness, in terms of γ [(28)] or width F_w [(29)], however, generally deviates from field observations (e.g., Donelan et al. 1985; Krivinskii 1991; Babanin and Soloviev 1998a) (Figs. 7 and 8). In particular, the peak of $E(f)$ from ST6^G and ST6^w appears too narrow, consistent with the finding of the recent numerical study by Annenkov and Shrira (2018).

5) A few problems presented here still remain unsolved, including that 1) the spectral narrowness F_n and directional spreading σ_θ are quite poorly resolved in the global simulations, as shown in Figs. 14 and 17; 2) wave models are able, to some degree, to present bimodal structure of short waves (Fig. 10); the lobe ratio r_{lobe}, however, is considerably underestimated (SOM); and 3) the model bias in the Southern Ocean is still relatively high ($b_n \sim 10\%$). All these issues are left for future research.

Finally, we conclude this study with the following recommendations:

1) ST6^D and ST4^D provide good, and very close, performance in estimating the commonly used integral wave parameters (significant wave height H_s, wave periods, mean square slope $\langle s^2 \rangle$ etc.), and therefore either of the two is applicable to the operational wave forecasting and hindcasting. Perrie et al. (2018) demonstrated that in their high-resolution wave forecast model systems, ST4^D outperformed the physics package originally designed for the WAM model (Hasselmann et al. 1988) but at the expense of at least 50% more CPU time. Considering the slightly higher computational efficiency of ST6^D in the 1-yr global hindcast (Table 4), we expect that ST6^D may save noticeable computational costs in such refined, high-resolution applications.
2) The wave spectrum of short gravity waves is crucial to estimate the wave-induced momentum flux from wind (e.g., Chalikov and Rainchik 2011). Since ST6 yields an improved high-frequency tail, it is recommended to further test/verify this package in the fully coupled atmosphere–wave–ocean models (e.g., Fan et al. 2009a; Warner et al. 2010; Chen et al. 2013).
3) The ST6^G model configuration (five quadruplets) increases computational costs by a factor of about 6, restricting its applicability to research purposes only, at least at this stage. For academic studies particularly concerned with low-frequency wave energy, ST6^G is preferred over ST6^D.
4) Only deep-water waves are considered in our present study. A thorough validation of the updated ST6 configurations in the finite-deep and shallow waters, similar to the work conducted by Aijaz et al. (2016) and van Vledder et al. (2016), is recommended for further analyses.

TABLE 4. The normalized model run time for 1-month global hindcast using the model setup summarized in section 5. The high-frequency limit $f_{h,f}$ of the prognostic region of the spectrum is defined by $f_{h,f} = N_{h,f}/T_{0,-1}$ (appendix A), where $N_{h,f} =$ — means the high-frequency spectral tail evolves freely without any prescribed slope. All the run times are normalized with the run time obtained with ST6^D and $N_{h,f} = 6$.

Model	$N_{h,f}$	Time
ST6^D	6	1.00
ST6^D	—	1.16
ST6^G	6	5.68
ST6^G	—	6.55
ST4^D	6	1.39

Acknowledgments. The authors are grateful to Dr. Kevin Ewans from MetOcean Research Ltd, New Zealand, for discussion about various aspects of wave spectra. The distribution and maintenance of WW3 and GMD codes by NOAA/NCEP is gratefully acknowledged. We appreciate Dr. David W. Wang from the U.S. Naval Research Laboratory for providing his code of the Maximum Entropy Method (MEM). QL, AVB, and IRY acknowledge the support from the DISI Australia–China Centre through Grant ACSRF48199. AVB also appreciates the financial support by ARC Discovery DP170101328. FQ is supported by the international cooperation project on the China–Australia Research Centre for Maritime Engineering of Ministry of Science and Technology, China under Grant 2016YFE0101400. We thank Dr. G. P. van Vledder and another reviewer for their detailed comments and suggestions that have improved our manuscript a lot.

APPENDIX A

Integral Parameters from the Wave Spectrum

The bulk parameters selected to evaluate wave model skills, including significant wave height H_s, mean wave period $T_{0,2}$, mean square slope $\langle s^2 \rangle$, mean wave direction θ_w, and directional spreading σ_θ, are calculated from the two-dimensional wave spectrum $F(f, \theta)$ as follows (see, e.g., T16 and Kuik et al. 1988):

$$
\begin{aligned}
m_n &= \int_{f_l}^{f_u}\int_0^{2\pi} f^n F(f,\theta)\, df\, d\theta,\\
H_s &= 4\sqrt{m_0},\\
T_{0,2} &= \sqrt{m_0/m_2},\\
T_{0,-1} &= m_{-1}/m_0,\\
\langle s^2 \rangle &= \int_{f_l}^{f_u}\int_0^{2\pi} k^2 F(f,\theta)\, df\, d\theta,\\
a &= \int_{f_l}^{f_u}\int_0^{2\pi} \cos\theta F(f,\theta)\, df\, d\theta,\\
b &= \int_{f_l}^{f_u}\int_0^{2\pi} \sin\theta F(f,\theta)\, df\, d\theta,\\
\theta_w &= \arctan(b/a),\\
\sigma_\theta &= \sqrt{2\left[1-\sqrt{(a^2+b^2)/m_0^2}\right]},
\end{aligned}
$$

where f_l and f_u are the lower and upper limits of integration. When wave models are verified against buoy observations, $f_l = 0.037$ Hz and $f_u = 0.485$ Hz are adopted. The peak period $T_p = 1/f_p$ is calculated from the omnidirectional frequency spectrum $E(f)$ using a parabolic fit in the neighborhood of the spectral peak. Following Ardhuin et al. (2010), the normalized bias b_n and ϵ_n are

$$
b_n = \sum_{i=1}^{N}(x_i - y_i)\Big/\sum_{i=1}^{N} y_i,
$$

$$
\epsilon_n = \sqrt{\sum_{i=1}^{N}(x_i - y_i)^2\Big/\sum_{i=1}^{N} y_i^2},
$$

where x_i and y_i are *simulated* and *measured* wave quantities, respectively. The other metrics, including bias b, RMSE ϵ, correlation coefficient ρ, scatter index SI, and normalized centered RMSE ϵ_n^c are calculated by their standard definitions [see, e.g., the appendix of Liu et al. (2017)] and thus are not described here.

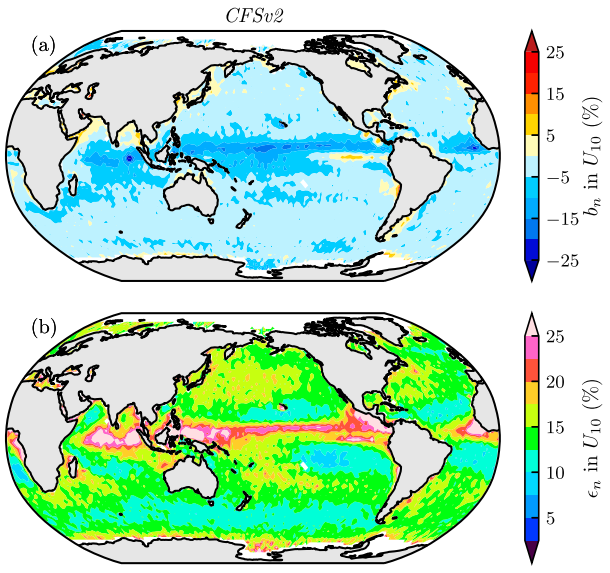

FIG. B1. As in Fig. 12, but for (a) the normalized bias b_n and (b) normalized RMSE ϵ_n of CFSv2 U_{10}, showing 2011 relative to altimeter measurements.

APPENDIX B

The Performance of the CFSv2 Winds

The performance of the CFSv2 winds of 2011 was carefully checked by SABZ16 (their section 2.3), using U_{10} measurements from the *Envisat* altimeter as the reference. Demonstrating the remarkably high accuracy of the CFSv2 wind forcing, SABZ16 showed the spatial distribution of the normalized bias b_n only in their Fig. 2. Motivated by our reviewers, here we provided the error maps of both b_n and ϵ_n in Fig. B1, which are helpful for explaining the wave model errors shown in Fig. 12. Altimeter U_{10} observations were sourced from the

multiple altimeter dataset (Young et al. 2017), and four altimeters (*Jason-1/2*, *Envisat*, and *CryoSat-2*) were selected.

REFERENCES

Aijaz, S., W. E. Rogers, and A. V. Babanin, 2016: Wave spectral response to sudden changes in wind direction in finite-depth waters. *Ocean Modell.*, **103**, 98–117, https://doi.org/10.1016/j.ocemod.2015.11.006.

Alves, J. H. G. M., and M. L. Banner, 2003: Performance of a saturation-based dissipation-rate source term in modeling the fetch-limited evolution of wind waves. *J. Phys. Oceanogr.*, **33**, 1274–1298, https://doi.org/10.1175/1520-0485(2003)033<1274:POASDS>2.0.CO;2.

——, ——, and I. R. Young, 2003: Revisiting the Pierson–Moskowitz asymptotic limits for fully developed wind waves. *J. Phys. Oceanogr.*, **33**, 1301–1323, https://doi.org/10.1175/1520-0485(2003)033<1301:RTPALF>2.0.CO;2.

——, S. Stripling, A. Chawla, H. L. Tolman, and A. J. van der Westhuysen, 2015: Operational wave guidance at the U.S. National Weather Service during Tropical/post–Tropical Storm Sandy, October 2012. *Mon. Wea. Rev.*, **143**, 1687–1702, https://doi.org/10.1175/MWR-D-14-00143.1.

Annenkov, S. Y., and V. I. Shrira, 2018: Spectral evolution of weakly nonlinear random waves: Kinetic description versus direct numerical simulations. *J. Fluid Mech.*, **844**, 766–795, https://doi.org/10.1017/jfm.2018.185.

Ardhuin, F., and A. D. Jenkins, 2006: On the interaction of surface waves and upper ocean turbulence. *J. Phys. Oceanogr.*, **36**, 551–557, https://doi.org/10.1175/JPO2862.1.

——, B. Chapron, and F. Collard, 2009: Observation of swell dissipation across oceans. *Geophys. Res. Lett.*, **36**, L06607, https://doi.org/10.1029/2008GL037030.

——, and Coauthors, 2010: Semiempirical dissipation source functions for ocean waves. Part I: Definition, calibration, and validation. *J. Phys. Oceanogr.*, **40**, 1917–1941, https://doi.org/10.1175/2010JPO4324.1.

——, J. Tournadre, P. Queffeulou, F. Girard-Ardhuin, and F. Collard, 2011: Observation and parameterization of small icebergs: Drifting breakwaters in the Southern Ocean. *Ocean Modell.*, **39**, 405–410, https://doi.org/10.1016/j.ocemod.2011.03.004.

Ataktürk, S. S., and K. B. Katsaros, 1999: Wind stress and surface waves observed on Lake Washington. *J. Phys. Oceanogr.*, **29**, 633–650, https://doi.org/10.1175/1520-0485(1999)029<0633:WSASWO>2.0.CO;2.

Babanin, A. V., 2006: On a wave-induced turbulence and a wave-mixed upper ocean layer. *Geophys. Res. Lett.*, **33**, L20605, https://doi.org/10.1029/2006GL027308.

——, 2010: Wind input, nonlinear interactions and wave breaking at the spectrum tail of wind-generated waves; transition from f^{-4} to f^{-5} behaviour. *Ecological Safety of Coastal and Shelf Zones and Comprehensive Use of Shelf Resources*, Vol. 21, Marine Hydrophysical Institute, 173–187.

——, 2011: *Breaking and Dissipation of Ocean Surface Waves.* Cambridge University Press, 480 pp., https://doi.org/10.1017/CBO9780511736162.

——, and Y. P. Soloviev, 1998a: Field investigation of transformation of the wind wave frequency spectrum with fetch and the stage of development. *J. Phys. Oceanogr.*, **28**, 563–576, https://doi.org/10.1175/1520-0485(1998)028<0563:FIOTOT>2.0.CO;2.

——, and ——, 1998b: Variability of directional spectra of wind-generated waves, studied by means of wave staff arrays. *Mar. Freshwater Res.*, **49**, 89–101, https://doi.org/10.1071/MF96126.

——, and I. R. Young, 2005: Two-phase behaviour of the spectral dissipation of wind waves. *Fifth Int. Symp. on Ocean Wave Measurements and Analysis (WAVES2005)*, Madrid, Spain, CEDEX, 51.

——, and B. K. Haus, 2009: On the existence of water turbulence induced by nonbreaking surface waves. *J. Phys. Oceanogr.*, **39**, 2675–2679, https://doi.org/10.1175/2009JPO4202.1.

——, I. R. Young, and M. L. Banner, 2001: Breaking probabilities for dominant surface waves on water of finite constant depth. *J. Geophys. Res.*, **106**, 11 659–11 676, https://doi.org/10.1029/2000JC000215.

——, M. L. Banner, I. R. Young, and M. A. Donelan, 2007: Wave-follower field measurements of the wind-input spectral function. Part III: Parameterization of the wind-input enhancement due to wave breaking. *J. Phys. Oceanogr.*, **37**, 2764–2775, https://doi.org/10.1175/2007JPO3757.1.

——, K. N. Tsagareli, I. R. Young, and D. J. Walker, 2010: Numerical investigation of spectral evolution of wind waves. Part II: Dissipation term and evolution tests. *J. Phys. Oceanogr.*, **40**, 667–683, https://doi.org/10.1175/2009JPO4370.1.

Banner, M. L., 1990: Equilibrium spectra of wind waves. *J. Phys. Oceanogr.*, **20**, 966–984, https://doi.org/10.1175/1520-0485(1990)020<0966:ESOWW>2.0.CO;2.

——, and I. R. Young, 1994: Modeling spectral dissipation in the evolution of wind waves. Part I: Assessment of existing model performance. *J. Phys. Oceanogr.*, **24**, 1550–1571, https://doi.org/10.1175/1520-0485(1994)024<1550:MSDITE>2.0.CO;2.

——, A. V. Babanin, and I. R. Young, 2000: Breaking probability for dominant waves on the sea surface. *J. Phys. Oceanogr.*, **30**, 3145–3160, https://doi.org/10.1175/1520-0485(2000)030<3145:BPFDWO>2.0.CO;2.

Battjes, J. A., T. J. Zitman, and L. H. Holthuusen, 1987: A reanalysis of the spectra observed in JONSWAP. *J. Phys. Oceanogr.*, **17**, 1288–1295, https://doi.org/10.1175/1520-0485(1987)017<1288:AROTSO>2.0.CO;2.

Booij, N., R. C. Ris, and L. H. Holthuijsen, 1999: A third-generation wave model for coastal regions: 1. Model description and validation. *J. Geophys. Res.*, **104**, 7649–7666, https://doi.org/10.1029/98JC02622.

Cavaleri, L., and Coauthors, 2007: Wave modelling—The state of the art. *Prog. Oceanogr.*, **75**, 603–674, https://doi.org/10.1016/j.pocean.2007.05.005.

——, and Coauthors, 2018: Wave modelling in coastal and inner seas. *Prog. Oceanogr.*, **167**, 164–233, https://doi.org/10.1016/j.pocean.2018.03.010.

Chalikov, D., and S. Rainchik, 2011: Coupled numerical modelling of wind and waves and the theory of the wave boundary layer. *Bound.-Layer Meteor.*, **138**, 1–41, https://doi.org/10.1007/s10546-010-9543-7.

Chen, S. S., W. Zhao, M. A. Donelan, and H. L. Tolman, 2013: Directional wind–wave coupling in fully coupled atmosphere–wave–ocean models: Results from CBLAST-Hurricane. *J. Atmos. Sci.*, **70**, 3198–3215, https://doi.org/10.1175/JAS-D-12-0157.1.

Delpey, M. T., F. Ardhuin, F. Collard, and B. Chapron, 2010: Space–time structure of long ocean swell fields. *J. Geophys. Res.*, **115**, C12037, https://doi.org/10.1029/2009JC005885.

Donelan, M. A., 2001: A nonlinear dissipation function due to wave breaking. *Proc. ECMWF Workshop on Ocean Wave Forecasting*, Reading, United Kingdom, ECMWF, 87–94.

——, 2017: Frequency–direction spectra of wind-generated gravity waves. *Encyclopedia of Maritime and Offshore Engineering*, J. Carlton, P. Jukes, and Y. S. Choo, Eds., John Wiley and Sons, https://doi.org/10.1002/9781118476406.emoe079.

——, J. Hamilton, and W. H. Hui, 1985: Directional spectra of wind-generated waves. *Philos. Trans. Roy. Soc.*, **315A**, 509–562, https://doi.org/10.1098/rsta.1985.0054.

——, A. V. Babanin, I. R. Young, M. L. Banner, and C. McCormick, 2005: Wave-follower field measurements of the wind-input spectral function. Part I: Measurements and calibrations. *J. Atmos. Oceanic Technol.*, **22**, 799–813, https://doi.org/10.1175/JTECH1725.1.

——, ——, ——, and ——, 2006: Wave-follower field measurements of the wind-input spectral function. Part II: Parameterization of the wind input. *J. Phys. Oceanogr.*, **36**, 1672–1689, https://doi.org/10.1175/JPO2933.1.

Ewans, K. C., 1998: Observations of the directional spectrum of fetch-limited waves. *J. Phys. Oceanogr.*, **28**, 495–512, https://doi.org/10.1175/1520-0485(1998)028<0495:OOTDSO>2.0.CO;2.

——, and A. C. Kibblewhite, 1990: An examination of fetch-limited wave growth off the west coast of New Zealand by a comparison with the JONSWAP results. *J. Phys. Oceanogr.*, **20**, 1278–1296, https://doi.org/10.1175/1520-0485(1990)020<1278:AEOFLW>2.0.CO;2.

Fan, Y., I. Ginis, and T. Hara, 2009a: The effect of wind–wave–current interaction on air–sea momentum fluxes and ocean response in tropical cyclones. *J. Phys. Oceanogr.*, **39**, 1019–1034, https://doi.org/10.1175/2008JPO4066.1.

——, ——, ——, C. W. Wright, and E. J. Walsh, 2009b: Numerical simulations and observations of surface wave fields under an extreme tropical cyclone. *J. Phys. Oceanogr.*, **39**, 2097–2116, https://doi.org/10.1175/2009JPO4224.1.

Forristall, G. Z., 1981: Measurements of a saturated range in ocean wave spectra. *J. Geophys. Res.*, **86**, 8075–8084, https://doi.org/10.1029/JC086iC09p08075.

Gramstad, O., and A. V. Babanin, 2016: The generalized kinetic equation as a model for the nonlinear transfer in third-generation wave models. *Ocean Dyn.*, **66**, 509–526, https://doi.org/10.1007/s10236-016-0940-4.

Hanley, K. E., S. E. Belcher, and P. P. Sullivan, 2010: A global climatology of wind–wave interaction. *J. Phys. Oceanogr.*, **40**, 1263–1282, https://doi.org/10.1175/2010JPO4377.1.

Hanson, J. L., and O. M. Phillips, 2001: Automated analysis of ocean surface directional wave spectra. *J. Atmos. Oceanic Technol.*, **18**, 277–293, https://doi.org/10.1175/1520-0426(2001)018<0277:AAOOSD>2.0.CO;2.

Hasselmann, K., 1962: On the non-linear energy transfer in a gravity-wave spectrum: Part 1. General theory. *J. Fluid Mech.*, **12**, 481–500, https://doi.org/10.1017/S0022112062000373.

——, 1963: On the non-linear energy transfer in a gravity-wave spectrum: Part 3. Evaluation of the energy flux and swell-sea interaction for a Neumann spectrum. *J. Fluid Mech.*, **15**, 385–398, https://doi.org/10.1017/S002211206300032X.

——, and Coauthors, 1973: Measurements of wind-wave growth and swell decay during the Joint North Sea Wave Project (JONSWAP). Tech. Rep., Deutches Hydrographisches Institut, 93 pp.

——, W. Sell, D. B. Ross, and P. Müller, 1976: A parametric wave prediction model. *J. Phys. Oceanogr.*, **6**, 200–228, https://doi.org/10.1175/1520-0485(1976)006<0200:APWPM>2.0.CO;2.

Hasselmann, S., and K. Hasselmann, 1985: Computations and parameterizations of the nonlinear energy transfer in a gravity-wave spectrum. Part I: A new method for efficient computations of the exact nonlinear transfer integral. *J. Phys. Oceanogr.*, **15**, 1369–1377, https://doi.org/10.1175/1520-0485(1985)015<1369:CAPOTN>2.0.CO;2.

——, ——, J. H. Allender, and T. P. Barnett, 1985: Computations and parameterizations of the nonlinear energy transfer in a gravity-wave spectrum. Part II: Parameterizations of the nonlinear energy transfer for application in wave models. *J. Phys. Oceanogr.*, **15**, 1378–1392, https://doi.org/10.1175/1520-0485(1985)015<1378:CAPOTN>2.0.CO;2.

——, and Coauthors, 1988: The WAM model—A third generation ocean wave prediction model. *J. Phys. Oceanogr.*, **18**, 1775–1810, https://doi.org/10.1175/1520-0485(1988)018<1775:TWMTGO>2.0.CO;2.

Holthuijsen, L. H., 2007: *Waves in Oceanic and Coastal Waters.* Cambridge University Press, 404 pp., https://doi.org/10.1017/CBO9780511618536.

Hwang, P. A., 2011: A note on the ocean surface roughness spectrum. *J. Atmos. Oceanic Technol.*, **28**, 436–443, https://doi.org/10.1175/2010JTECHO812.1.

——, and D. W. Wang, 2001: Directional distributions and mean square slopes in the equilibrium and saturation ranges of the wave spectrum. *J. Phys. Oceanogr.*, **31**, 1346–1360, https://doi.org/10.1175/1520-0485(2001)031<1346:DDAMSS>2.0.CO;2.

——, ——, E. J. Walsh, W. B. Krabill, and R. N. Swift, 2000a: Airborne measurements of the wavenumber spectra of ocean surface waves. Part I: Spectral slope and dimensionless spectral coefficient. *J. Phys. Oceanogr.*, **30**, 2753–2767, https://doi.org/10.1175/1520-0485(2001)031<2753:AMOTWS>2.0.CO;2.

——, ——, ——, ——, and ——, 2000b: Airborne measurements of the wavenumber spectra of ocean surface waves. Part II: Directional distribution. *J. Phys. Oceanogr.*, **30**, 2768–2787, https://doi.org/10.1175/1520-0485(2001)031<2768:AMOTWS>2.0.CO;2.

Janssen, P. A. E. M., 2003: Nonlinear four-wave interactions and freak waves. *J. Phys. Oceanogr.*, **33**, 863–884, https://doi.org/10.1175/1520-0485(2003)33<863:NFIAFW>2.0.CO;2.

——, 2004: *The Interaction of Ocean Waves and Wind.* Cambridge University Press, 312 pp., https://doi.org/10.1017/CBO9780511525018.

Kahma, K. K., and C. J. Calkoen, 1992: Reconciling discrepancies in the observed growth of wind-generated waves. *J. Phys. Oceanogr.*, **22**, 1389–1405, https://doi.org/10.1175/1520-0485(1992)022<1389:RDITOG>2.0.CO;2.

Komatsu, K., and A. Masuda, 1996: A new scheme of nonlinear energy transfer among wind waves: RIAM method-algorithm and performance. *J. Oceanogr.*, **52**, 509–537, https://doi.org/10.1007/BF02239052.

Komen, G. J., S. Hasselmann, and K. Hasselmann, 1984: On the existence of a fully developed wind-sea spectrum. *J. Phys. Oceanogr.*, **14**, 1271–1285, https://doi.org/10.1175/1520-0485(1984)014<1271:OTEOAF>2.0.CO;2.

——, L. Cavaleri, M. A. Donelan, K. Hasselmann, S. Hasselmann, and P. A. E. M. Janssen, 1994: *Dynamics and Modelling of Ocean Waves.* Cambridge University Press, 556 pp., https://doi.org/10.1017/CBO9780511628955.

Krivinskii, B. B., 1991: Variability of energetic characteristics of wind surface waves (in Russian). Ph.D. thesis, Marine Hydrophysical Institute, Ukrainian National Academy of Sciences, 191 pp.

Kuik, A. J., G. P. van Vledder, and L. H. Holthuijsen, 1988: A method for the routine analysis of pitch-and-roll buoy wave

data. *J. Phys. Oceanogr.*, **18**, 1020–1034, https://doi.org/10.1175/1520-0485(1988)018<1020:AMFTRA>2.0.CO;2.

Lenain, L., and W. K. Melville, 2017: Measurements of the directional spectrum across the equilibrium-saturation ranges of wind-generated surface waves. *J. Phys. Oceanogr.*, **47**, 2123–2138, https://doi.org/10.1175/JPO-D-17-0017.1.

Lewis, A., and R. Allos, 1990: JONSWAP's parameters: Sorting out the inconsistencies. *Ocean Eng.*, **17**, 409–415, https://doi.org/10.1016/0029-8018(90)90032-2.

Li, J.-G., 2012: Propagation of ocean surface waves on a spherical multiple-cell grid. *J. Comput. Phys.*, **231**, 8262–8277, https://doi.org/10.1016/j.jcp.2012.08.007.

——, and M. Holt, 2009: Comparison of *Envisat* ASAR ocean wave spectra with buoy and altimeter data via a wave model. *J. Atmos. Oceanic Technol.*, **26**, 593–614, https://doi.org/10.1175/2008JTECHO529.1.

Liu, Q., A. V. Babanin, Y. Fan, S. Zieger, C. Guan, and I.-J. Moon, 2017: Numerical simulations of ocean surface waves under hurricane conditions: Assessment of existing model performance. *Ocean Modell.*, **118**, 73–93, https://doi.org/10.1016/j.ocemod.2017.08.005.

Manasseh, R., A. V. Babanin, C. Forbes, K. Rickards, I. Bobevski, and A. Ooi, 2006: Passive acoustic determination of wave-breaking events and their severity across the spectrum. *J. Atmos. Oceanic Technol.*, **23**, 599–618, https://doi.org/10.1175/JTECH1853.1.

Nose, T., A. V. Babanin, and K. C. Ewans, 2017: In situ observations of infragravity wave directionality at nearshore coastal sites. *Ocean Sci. Discuss.*, https://doi.org/10.5194/os-2017-77.

Onorato, M., A. R. Osborne, M. Serio, L. Cavaleri, C. Brandini, and C. T. Stansberg, 2006: Extreme waves, modulational instability and second order theory: Wave flume experiments on irregular waves. *Eur. J. Mech.*, **25B**, 586–601, https://doi.org/10.1016/j.euromechflu.2006.01.002.

Perrie, W., B. Toulany, D. T. Resio, A. Roland, and J. P. Auclair, 2013: A two-scale approximation for wave–wave interactions in an operational wave model. *Ocean Modell.*, **70**, 38–51, https://doi.org/10.1016/j.ocemod.2013.06.008.

——, and Coauthors, 2018: Modeling North Atlantic nor'easters with modern wave forecast models. *J. Geophys. Res. Oceans*, **123**, 533–557, https://doi.org/10.1002/2017JC012868.

Pettersson, H., and K. Kahma, 2005: Directional measurements of wave growth in a short and narrow fetch geometry. *J. Atmos. Ocean Sci.*, **10**, 15–29, https://doi.org/10.1080/17417530500062853.

Phillips, O. M., 1958: The equilibrium range in the spectrum of wind-generated waves. *J. Fluid Mech.*, **4**, 426–434, https://doi.org/10.1017/S0022112058000550.

——, 1984: On the response of short ocean wave components at a fixed wavenumber to ocean current variations. *J. Phys. Oceanogr.*, **14**, 1425–1433, https://doi.org/10.1175/1520-0485(1984)014<1425:OTROSO>2.0.CO;2.

——, 1985: Spectral and statistical properties of the equilibrium range in wind-generated gravity waves. *J. Fluid Mech.*, **156**, 505–531, https://doi.org/10.1017/S0022112085002221.

Portilla, J., F. J. Ocampo-Torres, and J. Monbaliu, 2009: Spectral partitioning and identification of wind sea and swell. *J. Atmos. Oceanic Technol.*, **26**, 107–122, https://doi.org/10.1175/2008JTECHO609.1.

Rapizo, H., T. Waseda, A. V. Babanin, and A. Toffoli, 2016: Laboratory experiments on the effects of a variable current field on the spectral geometry of water waves. *J. Phys. Oceanogr.*, **46**, 2695–2717, https://doi.org/10.1175/JPO-D-16-0011.1.

——, A. V. Babanin, D. Provis, and W. E. Rogers, 2017: Current-induced dissipation in spectral wave models. *J. Geophys. Res. Oceans*, **122**, 2205–2225, https://doi.org/10.1002/2016JC012367.

——, T. H. Durrant, and A. V. Babanin, 2018: An assessment of the impact of surface currents on wave modeling in the Southern Ocean. *Ocean Dyn.*, **68**, 939–955, https://doi.org/10.1007/s10236-018-1171-7.

Rascle, N., and F. Ardhuin, 2013: A global wave parameter database for geophysical applications. Part 2: Model validation with improved source term parameterization. *Ocean Modell.*, **70**, 174–188, https://doi.org/10.1016/j.ocemod.2012.12.001.

Resio, D. T., and W. Perrie, 1991: A numerical study of nonlinear energy fluxes due to wave–wave interactions. Part 1: Methodology and basic results. *J. Fluid Mech.*, **223**, 603–629, https://doi.org/10.1017/S002211209100157X.

——, and ——, 2008: A two-scale approximation for efficient representation of nonlinear energy transfers in a wind wave spectrum. Part I: Theoretical development. *J. Phys. Oceanogr.*, **38**, 2801–2816, https://doi.org/10.1175/2008JPO3713.1.

——, C. E. Long, and C. L. Vincent, 2004: Equilibrium-range constant in wind-generated wave spectra. *J. Geophys. Res.*, **109**, C01018, https://doi.org/10.1029/2003JC001788.

——, L. Vincent, and D. Ardag, 2016: Characteristics of directional wave spectra and implications for detailed-balance wave modeling. *Ocean Modell.*, **103**, 38–52, https://doi.org/10.1016/j.ocemod.2015.09.009.

Ribal, A., A. V. Babanin, I. R. Young, A. Toffoli, and M. Stiassnie, 2013: Recurrent solutions of the Alber equation initialized by Joint North Sea Wave Project spectra. *J. Fluid Mech.*, **719**, 314–344, https://doi.org/10.1017/jfm.2013.7.

Rogers, W. E., 2017: Mean square slope in SWAN and WAVEWATCH III; buoy response functions; and limitations of ST1 physics in SWAN. *Waves in Shallow Water Environments Meeting (WISE-24)*, Victoria, BC, Canada, https://www7320.nrlssc.navy.mil/dynamic/posters/rogers.afterWISE2017.pdf.

——, and D. W. Wang, 2006: On validation of directional wave predictions: Review and discussion. Tech. Rep., Naval Research Laboratory, 38 pp., https://apps.dtic.mil/dtic/tr/fulltext/u2/a455737.pdf.

——, and ——, 2007: Directional validation of wave predictions. *J. Atmos. Oceanic Technol.*, **24**, 504–520, https://doi.org/10.1175/JTECH1990.1.

——, and G. P. van Vledder, 2013: Frequency width in predictions of windsea spectra and the role of the nonlinear solver. *Ocean Modell.*, **70**, 52–61, https://doi.org/10.1016/j.ocemod.2012.11.010.

——, P. A. Hwang, and D. W. Wang, 2003: Investigation of wave growth and decay in the SWAN model: Three regional-scale applications. *J. Phys. Oceanogr.*, **33**, 366–389, https://doi.org/10.1175/1520-0485(2003)033<0366:IOWGAD>2.0.CO;2.

——, A. V. Babanin, and D. W. Wang, 2012: Observation-consistent input and whitecapping dissipation in a model for wind-generated surface waves: Description and simple calculations. *J. Atmos. Oceanic Technol.*, **29**, 1329–1346, https://doi.org/10.1175/JTECH-D-11-00092.1.

Romero, L., and W. K. Melville, 2010a: Airborne observations of fetch-limited waves in the Gulf of Tehuantepec. *J. Phys. Oceanogr.*, **40**, 441–465, https://doi.org/10.1175/2009JPO4127.1.

——, and ——, 2010b: Numerical modeling of fetch-limited waves in the Gulf of Tehuantepec. *J. Phys. Oceanogr.*, **40**, 466–486, https://doi.org/10.1175/2009JPO4128.1.

——, L. Lenain, and W. K. Melville, 2017: Observations of surface wave–current interaction. *J. Phys. Oceanogr.*, **47**, 615–632, https://doi.org/10.1175/JPO-D-16-0108.1.

Saha, S., and Coauthors, 2014: The NCEP Climate Forecast System version 2. *J. Climate*, **27**, 2185–2208, https://doi.org/10.1175/JCLI-D-12-00823.1.

Stopa, J. E., F. Ardhuin, A. Babanin, and S. Zieger, 2016: Comparison and validation of physical wave parameterizations in spectral wave models. *Ocean Modell.*, **103**, 2–17, https://doi.org/10.1016/j.ocemod.2015.09.003.

SWAN Team, 2018: SWAN Scientific and technical documentation: SWAN cycle III version 41.20AB. Delft University of Technology Rep., 139 pp., http://swanmodel.sourceforge.net/download/zip/swantech.pdf.

Tamura, H., T. Waseda, Y. Miyazawa, and K. Komatsu, 2008: Current-induced modulation of the ocean wave spectrum and the role of nonlinear energy transfer. *J. Phys. Oceanogr.*, **38**, 2662–2684, https://doi.org/10.1175/2008JPO4000.1.

Taylor, K. E., 2001: Summarizing multiple aspects of model performance in a single diagram. *J. Geophys. Res.*, **106**, 7183–7192, https://doi.org/10.1029/2000JD900719.

Teixeira, M. A., and S. E. Belcher, 2002: On the distortion of turbulence by a progressive surface wave. *J. Fluid Mech.*, **458**, 229–267, https://doi.org/10.1017/S0022112002007838.

Toba, Y., 1973: Local balance in the air–sea boundary processes. III. On the spectrum of wind waves. *J. Oceanogr. Soc. Japan*, **29**, 209–220, https://doi.org/10.1007/BF02108528.

Tolman, H. L., 1991: A third-generation model for wind waves on slowly varying, unsteady, and inhomogeneous depths and currents. *J. Phys. Oceanogr.*, **21**, 782–797, https://doi.org/10.1175/1520-0485(1991)021<0782:ATGMFW>2.0.CO;2.

——, 1992: Effects of numerics on the physics in a third-generation wind-wave model. *J. Phys. Oceanogr.*, **22**, 1095–1111, https://doi.org/10.1175/1520-0485(1992)022<1095:EONOTP>2.0.CO;2.

——, 2003: Treatment of unresolved islands and ice in wind wave models. *Ocean Modell.*, **5**, 219–231, https://doi.org/10.1016/S1463-5003(02)00040-9.

——, 2010: Optimum discrete interaction approximations for wind waves. Part 4: Parameter optimization. Tech. Rep. 288, Environmental Modeling Center, Marine Modeling and Analysis Branch, 175 pp., http://polar.ncep.noaa.gov/mmab/papers/tn288/MMAB_288.pdf.

——, 2011: A conservative nonlinear filter for the high-frequency range of wind wave spectra. *Ocean Modell.*, **39**, 291–300, https://doi.org/10.1016/j.ocemod.2011.05.004.

——, 2013: A generalized multiple discrete interaction approximation for resonant four-wave interactions in wind wave models. *Ocean Modell.*, **70**, 11–24, https://doi.org/10.1016/j.ocemod.2013.02.005.

——, and D. Chalikov, 1996: Source terms in a third-generation wind wave model. *J. Phys. Oceanogr.*, **26**, 2497–2518, https://doi.org/10.1175/1520-0485(1996)026<2497:STIATG>2.0.CO;2.

——, and R. W. Grumbine, 2013: Holistic genetic optimization of a generalized multiple discrete interaction approximation for wind waves. *Ocean Modell.*, **70**, 25–37, https://doi.org/10.1016/j.ocemod.2012.12.008.

Tracy, B., and D. T. Resio, 1982: Theory and calculation of the nonlinear energy transfer between sea waves in deep water. WES Rep. 11, U.S. Army Corps of Engineers, 56 pp., http://www.dtic.mil/dtic/tr/fulltext/u2/a117989.pdf.

Tsagareli, K. N., A. V. Babanin, D. J. Walker, and I. R. Young, 2010: Numerical investigation of spectral evolution of wind waves. Part I: Wind-input source function. *J. Phys. Oceanogr.*, **40**, 656–666, https://doi.org/10.1175/2009JPO4345.1.

van der Westhuysen, A. J., M. Zijlema, and J. A. Battjes, 2007: Nonlinear saturation-based whitecapping dissipation in SWAN for deep and shallow water. *Coastal Eng.*, **54**, 151–170, https://doi.org/10.1016/j.coastaleng.2006.08.006.

van Vledder, G. P., 2006: The WRT method for the computation of non-linear four-wave interactions in discrete spectral wave models. *Coastal Eng.*, **53**, 223–242, https://doi.org/10.1016/j.coastaleng.2005.10.011.

——, S. T. Hulst, and J. D. McConochie, 2016: Source term balance in a severe storm in the southern North Sea. *Ocean Dyn.*, **66**, 1681–1697, https://doi.org/10.1007/s10236-016-0998-z.

Wang, D. W., and P. A. Hwang, 2001: Evolution of the bimodal directional distribution of ocean waves. *J. Phys. Oceanogr.*, **31**, 1200–1221, https://doi.org/10.1175/1520-0485(2001)031<1200:EOTBDD>2.0.CO;2.

Warner, J. C., B. Armstrong, R. He, and J. B. Zambon, 2010: Development of a Coupled Ocean–Atmosphere–Wave–Sediment Transport (COAWST) modeling system. *Ocean Modell.*, **35**, 230–244, https://doi.org/10.1016/j.ocemod.2010.07.010.

WAVEWATCH III Development Group, 2016: User manual and system documentation of WAVEWATCH III version 5.16. Environmental Modeling Center, Marine Modeling and Analysis Branch, NCEP, 360 pp., http://polar.ncep.noaa.gov/waves/wavewatch/manual.v5.16.pdf.

Webb, D. J., 1978: Non-linear transfers between sea waves. *Deep-Sea Res.*, **25**, 279–298, https://doi.org/10.1016/0146-6291(78)90593-3.

Xiao, W., Y. Liu, G. Wu, and D. K. Yue, 2013: Rogue wave occurrence and dynamics by direct simulations of nonlinear wave-field evolution. *J. Fluid Mech.*, **720**, 357–392, https://doi.org/10.1017/jfm.2013.37.

Young, I. R., 1999: *Wind Generated Ocean Waves.* Elsevier Science Ltd., 287 pp.

——, 2006: Directional spectra of hurricane wind waves. *J. Geophys. Res.*, **111**, C08020, https://doi.org/10.1029/2006JC003540.

——, and G. P. van Vledder, 1993: A review of the central role of nonlinear interactions in wind-wave evolution. *Philos. Trans. Roy. Soc. London*, **342A**, 505–524, https://doi.org/10.1098/rsta.1993.0030.

——, and A. V. Babanin, 2006: Spectral distribution of energy dissipation of wind-generated waves due to dominant wave breaking. *J. Phys. Oceanogr.*, **36**, 376–394, https://doi.org/10.1175/JPO2859.1.

——, S. Hasselmann, and K. Hasselmann, 1987: Computations of the response of a wave spectrum to a sudden change in wind direction. *J. Phys. Oceanogr.*, **17**, 1317–1338, https://doi.org/10.1175/1520-0485(1987)017<1317:COTROA>2.0.CO;2.

——, L. A. Verhagen, and M. L. Banner, 1995: A note on the bimodal directional spreading of fetch-limited wind waves. *J. Geophys. Res.*, **100**, 773–778, https://doi.org/10.1029/94JC02218.

——, M. L. Banner, M. A. Donelan, C. McCormick, A. V. Babanin, W. K. Melville, and F. Veron, 2005: An integrated system for the study of wind-wave source terms in finite-depth water. *J. Atmos. Oceanic Technol.*, **22**, 814–831, https://doi.org/10.1175/JTECH1726.1.

——, A. V. Babanin, and S. Zieger, 2013: The decay rate of ocean swell observed by altimeter. *J. Phys. Oceanogr.*, **43**, 2322–2333, https://doi.org/10.1175/JPO-D-13-083.1.

——, E. Sanina, and A. V. Babanin, 2017: Calibration and cross validation of a global wind and wave database of altimeter, radiometer, and scatterometer measurements. *J. Atmos. Oceanic Technol.*, **34**, 1285–1306, https://doi.org/10.1175/JTECH-D-16-0145.1.

Zakharov, V. E., 1968: Stability of periodic waves of finite amplitude on the surface of a deep fluid. *J. Appl. Mech. Tech. Phys.*, **9**, 190–194, https://doi.org/10.1007/BF00913182.

——, 2018: Analytic theory of a wind-driven sea. *Procedia IUTAM*, **26**, 43–58, https://doi.org/10.1016/j.piutam.2018.03.005.

Zieger, S., A. V. Babanin, W. E. Rogers, and I. R. Young, 2015: Observation-based source terms in the third-generation wave model WAVEWATCH. *Ocean Modell.*, **96**, 2–25, https://doi.org/10.1016/j.ocemod.2015.07.014.